2018

Robust Power Interface for Smart Grid with Renewable Energy Source-to-Grid Functionality

BoHyun Ahn
Minnesota State University, Mankato

Robust Power Interface for Smart Grid with Renewable Energy Source-to-Grid Functionality

A THESIS

SUBMITTED TO THE GRADUATE SCHOOL OF

MINNESOTA STATE UNIVERSITY, MANKATO

BY

BoHyun Ahn

IN PARTIAL FULFILLMENT OF THE REQUIREMENTS

FOR THE DEGREE OF

Master of Science in Electrical Engineering

Advisor: Dr. Vincent Winstead, Ph.D., P.E.

December, 2018

Robust Power Interface for Smart Grid with

Renewable Energy Source-to-Grid Functionality

A THESIS PRESENTED

BY

BoHyun Ahn

Approved as to style and content by:

Vincent Winstead, Ph.D., P.E.

Advisor, Professor of Electrical and Computer Engineering and Technology

---

Han-Way Huang, Ph.D.

Professor of Electrical and Computer Engineering and Technology

---

Xuanhui Wu, Ph.D.

Associate Professor of Electrical and Computer Engineering and Technology

Acknowledgements

It is my honor and distinct pleasure to thank the many people who have guided me through my graduate schooling. I sincerely do not have the words to thank you to my advisor, Professor Vincent Winstead, for guiding me from undergraduate to master's program, giving me the opportunity to join his renewable energy research team. I feel honored to be a student of Professor Winstead's.

I would like to thank my committee members, Professor Han-Way Huang and Professor Xuanhui Wu.

Special thanks to Professor Jianwu Zeng for advice about power electronics and software problems.

I would like to thank my parents and my fiancé who have believed in me from the start and provided unfailing love and support.

Dedication

This thesis is dedicated to God, my parents Sang-Ho Ahn and Gyeong-Sook Baek, my sister So-Young Ahn, my godparents Dean Bowyer and Cheri Bowyer, my fiancé Hara Goo, and the rest of my friends. I would have never accomplished what I have without the huge support system of family. I am blessed to have them and for that I am eternally grateful.

Abstract

Many renewable energy companies design wind turbine generators, solar panels, or electrical car batteries with different specifications according to their management philosophy. And typical commercial power converters are not universally designed for all different types of renewable energy systems. Because of this lack of flexibility and interoperability, a universal and scalable smart grid power converter design is desirable. Designing a robust controlled bi-directional power converter is the motivation for this thesis as the first step to develop a more universal converter topology connecting renewable energy sources and the electrical smart-grid of the future.

Renewable energy such as wind or solar power are promising alternatives with many advantages to traditional energy sources but they cannot provide a constant power flow due to the inherent variability of weather. For example, wind speed fluctuates depending on its elevation and solar irradiance fluctuates when moving clouds cover the sun. These example scenarios can be considered as uncertainty and one can assume that uncertainty is time varying as well. For these reasons, it is clear that wind turbine generators and solar panels cannot generate constant power levels and it may result in malfunctions in the converter and instability in the grid.

Traditional and modern control theories, such as PID controllers, are not always tolerant to changes in the environment. Thus, the application of a robust control theory, such as a H_∞ control technique, is proposed. The objective of this thesis is to compare an H_∞ robust controller to a PI controller. To apply the controllers, a plant consisting of a bi-directional AC/DC Dual-Active-Bridge (DAB) converter topology is studied and presented. This topology was recently proposed by N. D. Weise et al [1] and [4]. Also, to design the controllers, a small signal approach based on the converter topology to provide a transfer function generated from a model averaging process is obtained.

The presented converter has continuous-time behavior with discrete switching events. Thus, this converter can be described by the properties of switched systems which are subordinate to hybrid systems. To verify the stability of the switched converter system, a continuous Lyapunov function is constructed.

Results from the model are compared against the simulation results and theory. Different control strategies are presented and compared.

Contents

Acknowledgements ..... **i**

Dedication ..... **ii**

Abstract ..... **iii**

List of Tables ..... **vii**

List of Figures ..... **viii**

1 Introduction **1**

2 AC/DC Dual-Active-Bridge Analysis **3**

2.1 Analysis 3

2.2 Simulation 12

2.3 Conclusion 18

3 Small-signal System Model Analysis **19**

3.1 Analysis 19

3.2 Simulation 23

3.3 Conclusion 27

4 Robust Control Analysis **28**

4.1 Analysis 28

4.2 Simulation 35

4.3 Conclusion 41

5 Hybrid System Model Analysis **42**

5.1 Analysis 42

5.2 Simulation 46

5.3 Conclusion 51

Conclusion **52**

References **53**

Appendix A. Leakage Inductance **58**

List of Tables

Table 2.1: Simulation Parameters. 12

Table 5.1: Simulation Parameters. 46

List of Figures

Fig. 2.1: Topology of the proposed converter. 3
Fig. 2.2: Switching sequence within period T_S for the AC-side H-bridge components. 5
Fig. 2.3: Switching sequence within period T_S for the DC-side H-bridge components. 6
Fig. 2.4: Modulation cycle of one switching period when the AC source voltage swings positive ($vi(t) > 0$)....8
Fig. 2.5: Sinusoidal Pulse Width Modulation. 10
Fig. 2.6: Simulation results when phase shift ratio is positive (+0.3). 15

Fig. 3.1: Plot of X(t) over a single input waveform cycle. 24
Fig. 3.2: Plot of X(t) over a single switching period. 25
Fig. 3.3: Plot of $X + x(t)$ over a single input waveform cycle. 26

Fig. 4.1: Simple closed-loop control system. 29
Fig. 4.2: H_∞ controller design for the converter. 33
Fig. 4.3: Block Diagram of augw function in MATLAB. 36
Fig. 4.4: Step Response of G(s). 37

Fig. 5.1: A Simple Mechanism of a Hybrid System. 42
Fig. 5.2: Two and Half Cycles. 46

Chapter 1

Introduction

Renewable energy such as wind power, solar power, and the use of biofuels are promising alternatives to traditional energy sources derived from oil and gas, and promises to positively impact global climate change reducing the effects due to the combustion of fossil fuels mostly in cars, factories and power plants. Electrical power converters allow for the transfer of power and improve power quality between renewable energy sources and the electrical grid. For high efficiency and power density with bi-directional power flow, Dual-Active-Bridge (DAB) single-stage AC/DC converters have been proposed in [1], [2], [3], [4], and [5]. The analysis of the AC/DC DAB converter in [1], [2], and [3] was implemented under open-loop conditions. A Proportional Integral (PI) controller for control to the converter was introduced in [4]. And, a DQ controller was applied to the converter in [5] and [6]. In wind turbine systems, uncertainty arises at all points in the process, from measuring the wind speed to the uncertainty in a power curve due to wind speed fluctuations and weather conditions [7]. The previously mentioned control algorithms are not always tolerant to changes in the environment [8]. H_∞ robust control theory seeks to impose a bound on the uncertainty in the form of minimizing a system norm derived through uncertainty modeling [10], [19], [20], [21], [22], [23], [24], [25] and [26]. However, control methodologies such as those based on H_∞ can be

computationally expensive. For designing the closed-loop H_∞ control system, a dynamic plant model of the converter should be obtained first. The plant modeling component is approached through the derivation of a small-signal plant model using a state-space averaging technique introduced in [9], [13], [14], [15], [16], [17] and [18]. The goal of this thesis is to compare multiple control architectures including H_∞ robust controller and PI controller to the designed plant modeling. Then the stability of the plant will be verified by the construction of Lyapunov function [27], [28], [29], and [30].

Chapter 2

AC/DC Dual-Active-Bridge Analysis

2.1 Analysis

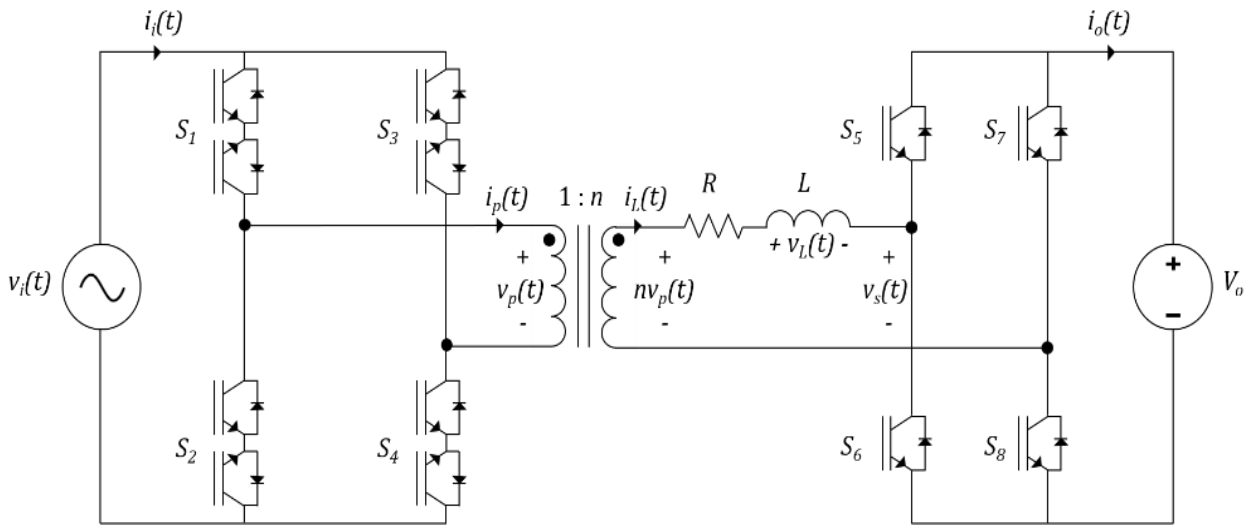

Fig. 2.1: Topology of the proposed converter.

Fig. 2.1 shows the topology of the proposed converter. This is the single-stage DAB bi-directional AC/DC converter. The proposed converter is similar to that found previously in the literature [1]

and [4], however, we incorporate a lumped resistance on the transformer secondary side to provide enhanced model accuracy. In Fig. 2.1, the primary side H-bridge is connected to an input AC source with voltage $v_i(t)$ at an input frequency f_i with a peak magnitude of input voltage V_i, i.e. $v_i(t) = V_i \cdot sin(\omega t) = V_i \cdot sin(2\pi f_i t)$.

The switches S_1, S_2, S_3, and S_4 on the primary side H-bridge (the AC side) are four-quadrant switches and are realized with emitter tied IGBTs. It must be four-quadrant because the AC source voltage swings both positive and negative. The switches are operated by digital pulses at a switching frequency f_s. During the first half switching period $\frac{T_s}{2} = \frac{\frac{1}{f_s}}{2} = \frac{1}{2 \cdot f_s}$, S_1 and S_4 are on and S_2 and S_3 are off. In this period, positive $v_i(t)$ is applied to $v_p(t)$ at the primary side of the transformer then positive $nv_i(t)$ is applied to $nv_p(t)$ where the secondary side of the transformer. During the second half switching period, S_1 and S_4 are off and S_2 and S_3 are on. In this period, negative $v_i(t)$ is applied to $v_p(t)$ at the primary side of the transformer. Then negative $nv_p(t)$ is observed on the secondary side. In other words, the states are on and off for 50% of one switching period $T_s = \frac{1}{f_s}$. The waveform of the two switching states at $v_p(t)$ is depicted in Fig. 2.2.

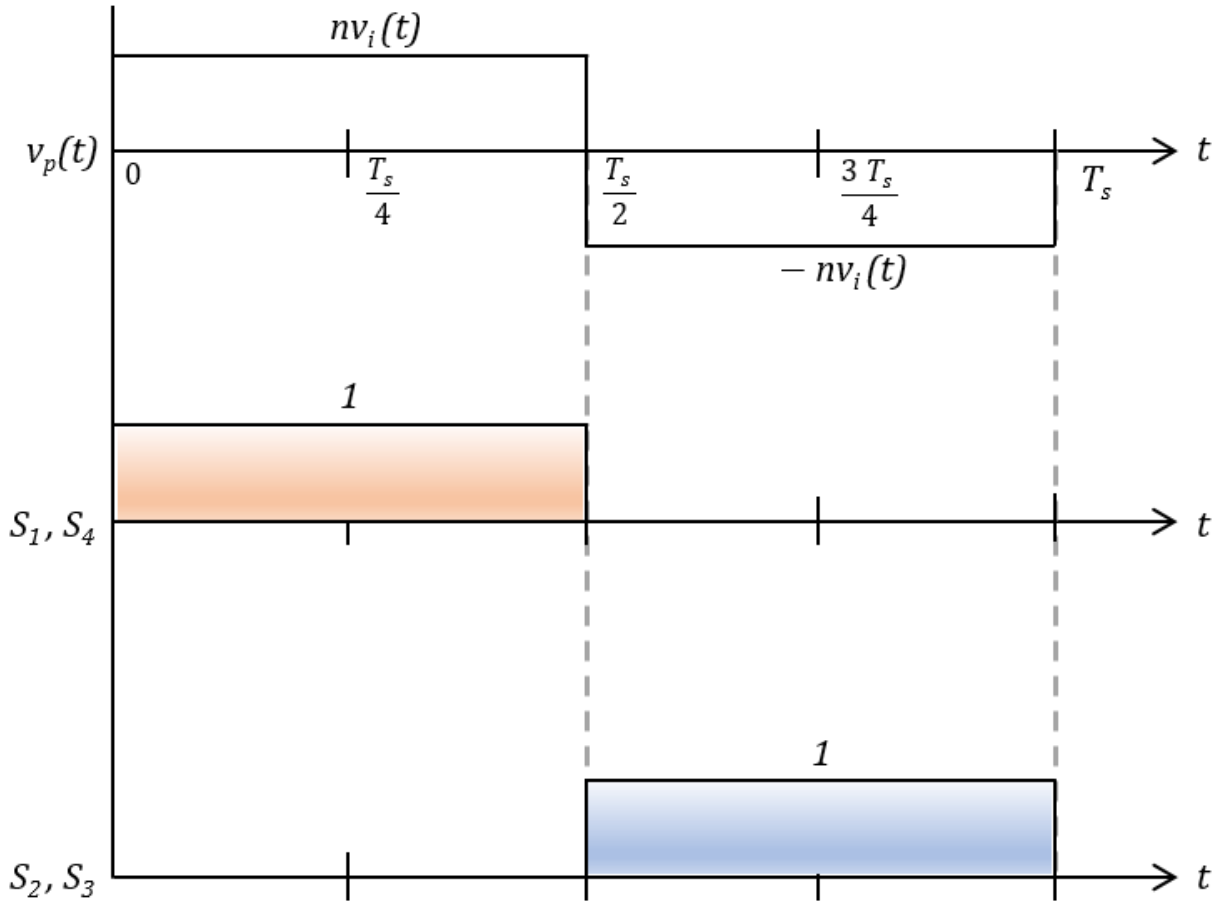

Fig. 2.2: Switching sequence within period T_s for the AC-side H-bridge components.

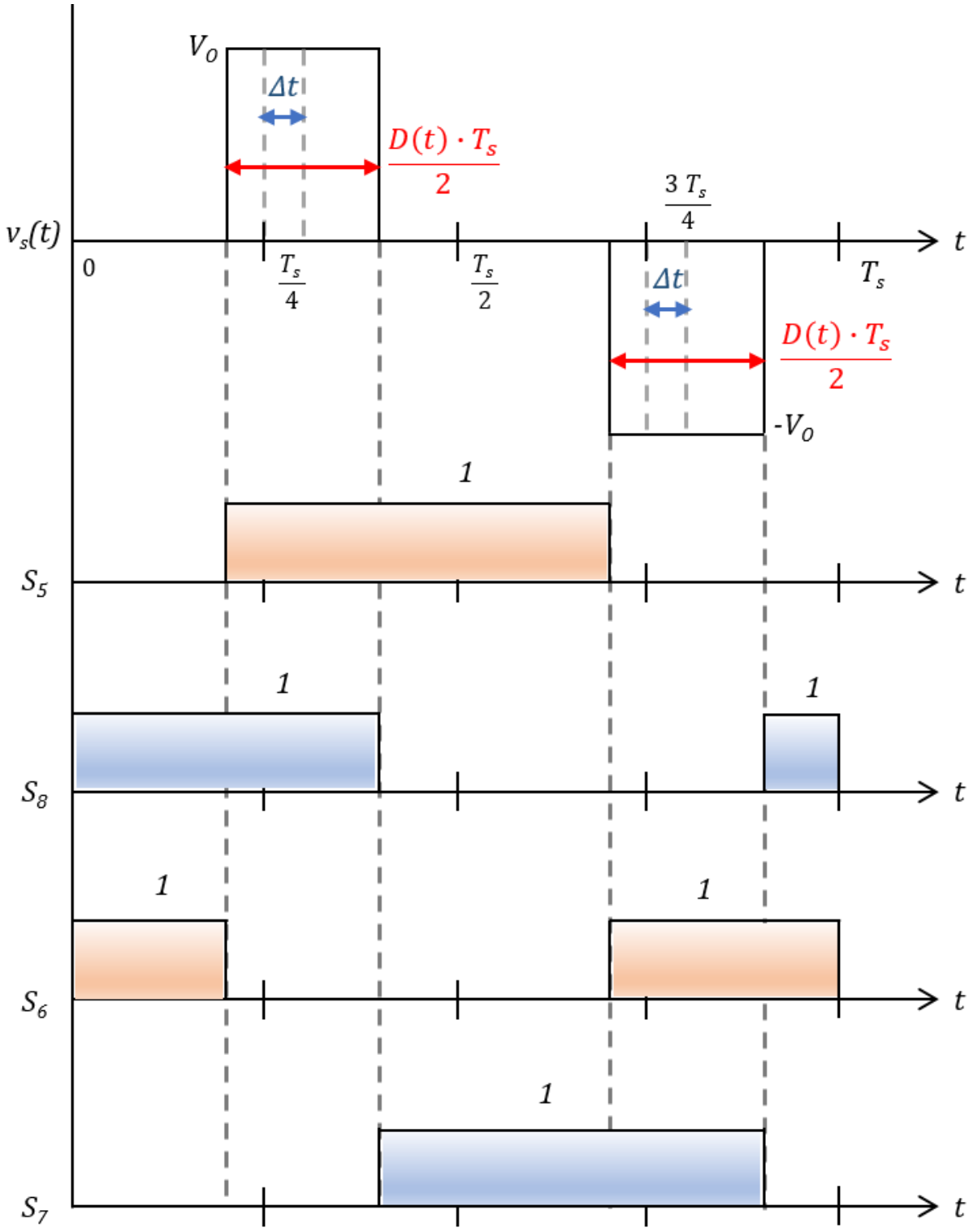

Fig. 2.3: Switching sequence within period T_s for the DC-side H-bridge components.

The switches S_5, S_6, S_7, and S_8 on the secondary side H-bridge (the DC-side) are two-quadrant switches and components are assumed to be ideal. In Fig. 2.3, when the switches S_5 and S_8 are on and the switches S_6 and S_7 are off simultaneously, positive V_O is applied to $v_s(t)$. When the switches S_5 and S_8 are off and the switches S_6 and S_7 are on simultaneously, negative V_O is applied to $v_s(t)$. In the rest of the switching cases, zero voltage is applied to $v_s(t)$.

The pulse width of $v_s(t)$ is defined by time-varying duty ratio, $D(t)$. Within period T_s, the voltage waveform, $v_s(t)$, must be phase shifted, by Δt (see Fig 2.3), in order to control power transfer. The first and second plots of Fig. 2.4 show the comparison between the waveform at $v_p(t)$ and the phase shifted waveform at $v_s(t)$. Here, the waveform at $v_s(t)$ must stay inside of the waveform at $v_p(t)$. When Δt is assigned as positive, power flows from AC source to DC source. When Δt is assigned as negative, power flows from DC source to AC source.

In this analysis, the turns ratio of the transformer is assumed to be one and the magnetizing inductance, and cores losses of the transformer are all neglected. Thus, this transformer can be considered as an ideal transformer. The proposed modulation scheme utilizes the leakage inductance of the transformer to transfer power in the topology shown in Fig. 1. The transformer has a turns ratio of $1:n$ and the primary and secondary leakage inductance, L, is connected to the secondary side as $L = L_P n^2 + L_s$, for analysis. The concept of the leakage inductance is described in detail in Appendix A and [32]. The small-valued resistor representing the lumped resistance, R, is added to enhance the accuracy of the model and facilitates a state-space average modeling for analysis and designing a small-signal transfer function. The secondary side H-bridge is connected to a DC source with voltage V_o.

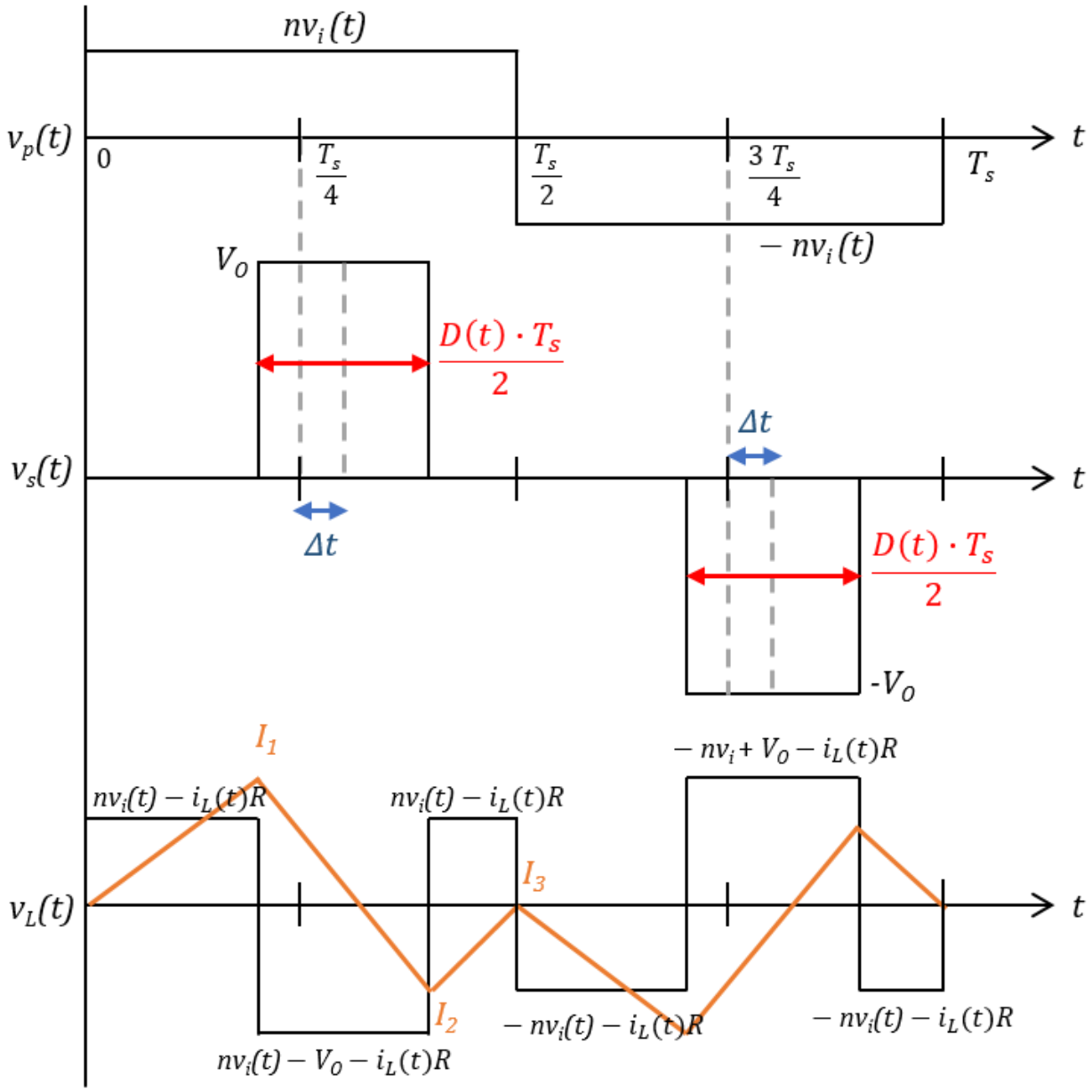

Fig. 2.4: Modulation cycle of one switching period when the AC source voltage swings positive ($v_i(t) > 0$).

The input AC voltage source, $v_i(t)$, on the AC-side H-bridge is defined in equation (2.1).

$$v_i(t) = V_i sin(2\pi f_i t). \tag{2.1}$$

On the primary side of the transformer, the primary voltage pulse, $v_p(t)$, is applied by the AC-

side H-bridge with 50% pulse width of the switching period. The parameter $v_p(t)$ is defined in equation (2.2).

$$nv_p(t) = \begin{cases} nv_i(t); & 0 < t < \frac{T_s}{2} \\ -nv_i(t); & \frac{T_s}{2} < t < T_s \end{cases} . \quad (2.2)$$

On the secondary side of the transformer, the secondary voltage pulse, $v_s(t)$, is applied by the DC-side H-bridge with a phase shifted time-varying duty ratio. The time-varying duty ratio, $D(t)$ is defined in equation (2.3).

$$D(t) = \frac{n|v_i(t)|}{V_o} = \frac{n\cdot(sign[v_i(t)]\cdot v_i(t))}{V_o} , \quad (2.3)$$

where

$$sgn(v_i(t)) = \begin{cases} +1; & v_i(t) > 0 \\ 0; & v_i(t) = 0 \\ -1; & v_i(t) < 0 \end{cases}$$

The peak duty ratio is defined as $\widehat{D}(t) = \frac{nV_i}{V_o}$. Here, given n and $v_i(t)$, V_i and V_o are selected to keep $D(t) < 1$. For modulation regarding the time-varying duty ratio, the sinusoidal pulse width modulation (SPWM) technique is applied [11], [12].

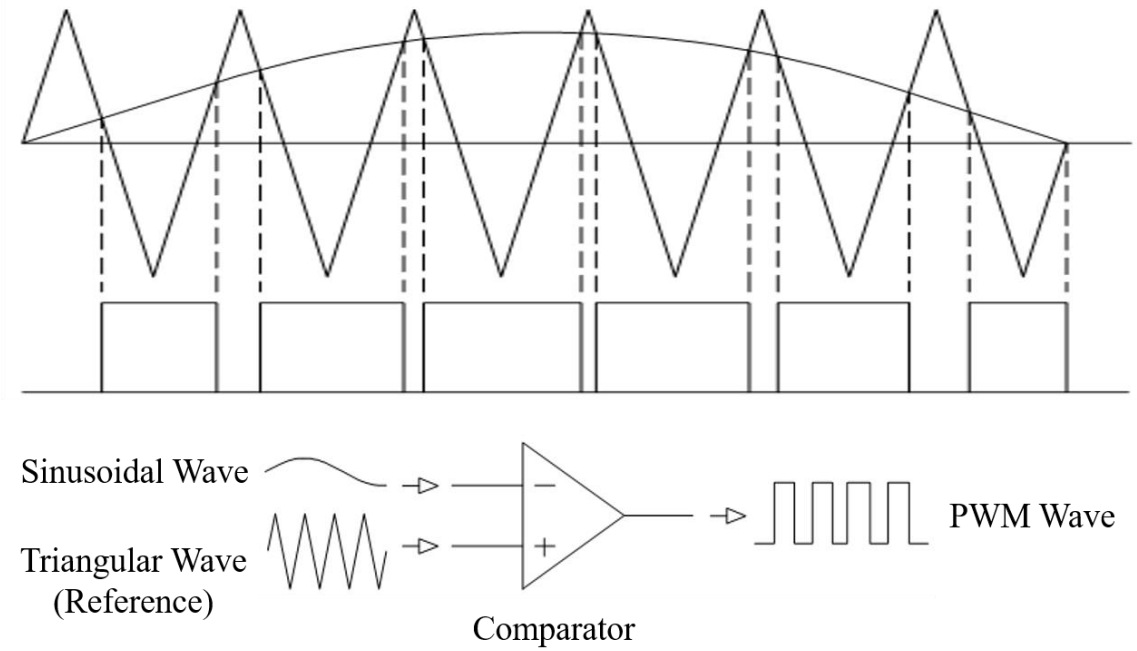

Fig. 2.5: Sinusoidal Pulse Width Modulation.

A sinusoidal wave is compared with a reference triangular wave. Here, the frequency of the triangular wave is higher than the sinusoidal wave. Comparing two waves using a comparator, when the magnitude of sinusoidal wave is higher than the triangular wave, the digital value of the comparator output is 1. Otherwise, it is zero. From this process, a PWM wave, which has variable pulse width, is generated.

Furthermore, the phase shift, Δt, is defined in equation (2.4), where δ is a phase shift ratio and satisfies $|\delta| \leq (1 - D(t))$.

$$\Delta t = \frac{\delta \cdot T_s}{4} \ . \tag{2.4}$$

Thus, $v_s(t)$ can be defined over a single complete switching period, T_s.

$$v_s(t) = \begin{cases} 0; & 0 \le t < \frac{T_s}{4}(1+\delta-D(t)) \\ sgn\big(v_i(t)\big)\cdot V_o; & \frac{T_s}{4}(1+\delta-D(t)) \le t < \frac{T_s}{4}(1+\delta+D(t)) \\ 0; & \frac{T_s}{4}(1+\delta+D(t)) \le t < \frac{3T_s}{4}+\frac{T_s}{4}(\delta-D(t)) \\ -sgn\big(v_i(t)\big)\cdot V_o; & \frac{3T_s}{4}+\frac{T_s}{4}(\delta-D(t)) \le t < \frac{3T_s}{2}+\frac{T_s}{4}(\delta+D(t)) \\ 0; & \frac{3T_s}{4}+\frac{T_s}{4}\big(\delta+D(t)\big) \le t < T_s. \end{cases} \quad (2.5)$$

Applying Kirchoff's Voltage Law (KVL), around the transformer in Fig. 2.1, yields the following:

$$v_L(t) = nv_p(t) - v_s(t) - i_L(t)R. \quad (2.6)$$

The inductor voltage, $v_L(t)$, can be defined as follows assuming that the inductor current is initially zero and $v_i(t)$ is positive. After applying equations (2.2) and (2.5) for each time interval of T_s, Equation (7) can be derived verifying the third plot in Fig. 2.4.

$$v_L(t) = L\frac{di_L(t)}{dt}$$

$$= \begin{cases} nv_i(t) - (0) - i_L(t)R, & 0 \le t < \frac{T_s}{4}(1+\delta-D) \\ nv_i(t) - (+V_o) - i_L(t)R, & \frac{T_s}{4}(1+\delta-D) \le t < \frac{T_s}{4}(1+\delta+D) \\ nv_i(t) - (0) - i_L(t)R, & \frac{T_s}{4}(1+\delta+D) \le t < \frac{T_s}{2} \\ -nv_i(t) - (0) - i_L(t)R, & \frac{T_s}{2} \le t < \frac{T_s}{2}+\frac{T_s}{4}(1+\delta-D) \\ -nv_i(t) - (-V_o) - i_L(t)R, & \frac{T_s}{2}+\frac{T_s}{4}(1+\delta-D) \le t < \frac{T_s}{2}+\frac{T_s}{4}(1+\delta+D) \\ -nv_i(t) - (0) - i_L(t)R, & \frac{T_s}{2}+\frac{T_s}{4}(1+\delta+D) \le t < T_s \end{cases}$$

$$= \begin{cases} nv_i(t) - i_L(t)R, & 0 \le t < \frac{T_s}{4}(1+\delta-D) \\ nv_i(t) - V_o - i_L(t)R, & \frac{T_s}{4}(1+\delta-D) \le t < \frac{T_s}{4}(1+\delta+D) \\ nv_i(t) - i_L(t)R, & \frac{T_s}{4}(1+\delta+D) \le t < \frac{T_s}{2} \\ -nv_i(t) - i_L(t)R, & \frac{T_s}{2} \le t < \frac{T_s}{2} + \frac{T_s}{4}(1+\delta-D) \\ -nv_i(t) + V_o - i_L(t)R, & \frac{T_s}{2} + \frac{T_s}{4}(1+\delta-D) \le t < \frac{T_s}{2} + \frac{T_s}{4}(1+\delta+D) \\ -nv_i(t) - i_L(t)R, & \frac{T_s}{2} + \frac{T_s}{4}(1+\delta+D) \le t < T_s. \end{cases} \quad (2.7)$$

According to Equation (2.7) and the third plot of Fig. 2.4, when the inductor, L, has positive voltage (charging), the current through the inductor (orange line), $i_L(t)$ increases linearly. Again, the resistor, R, is a small value. However, when the inductor has negative voltage (discharging), the inductor current decreases.

2.2 Simulation

Parameter	Value	Unit
n	1	
L	50	uH
R	0.1	Ohm
V_i	100	Volt
V_o	250	Volt
T_s	0.0001	s
δ	0.3	
f_i	60	Hz

Table 2.1: Simulation Parameters.

The simulation results are implemented by MATLAB and Simulink. The simulation results of the proposed converter in Fig. 2.1, with the SPWM technique and the simulation parameters given in Table 2.1, applied is shown in Fig. 2.6, and 2.7. In the Table 2.1, the phase shift ratio is defined as

δ. The peak value of the input AC source (V_i) is given 100 V and the output DC source (V_o) is set to 250 V. Because the input AC source frequency (f_i) is set to 60 Hz, one input cycle is 1/60 Hz = 0.0167 s. Fig 2.6 (a) shows the simulation result regarding one single input cycle when the phase shift ratio δ is positive (+0.3). And Fig. 2.7 (a) shows the simulation result when δ is negative (-0.3).

Regardless of the different sign of phase shift ratio, both simulation results show the DC output as 250 V (Blue), the AC input as 100 V peak (Green), and the Inductor current (Red). From 0 to 0.0083 sec, the green input sine wave swings positive, and, from 0.0083 sec to 0.0167 sec, the sine wave swings negative. Fig 2.6 (b)-(c) and Fig 2.7 (b)-(c) are zoom in from Fig 2.6 (a) and Fig 2.7 (b) separately. From equation (2.3) or looking at Fig 2.6 (a) and 2.7 (a), when the input AC source has a peak value, it shows the maximum duty ratio in Fig. 2.6 (b) and Fig. 2.7 (b) near 0.00425 sec on the plot, separately. Otherwise, it shows the minimum duty ratio in each Fig. 2.6 (c) and Fig 2.7 (c) near 0 sec on the plot.

Considering the direction of phase shift ratio, when δ is set to positive, the waveforms of the input AC voltage and the inductor current are in phase (Fig 2.6 (d)). This means the power flows from the AC source to the DC source. However, when δ is negative, the waveforms are 180 degree out of phase. In other words, the power is flowing from the DC source to the AC source and demonstrates the capability for bi-directional power transfer.

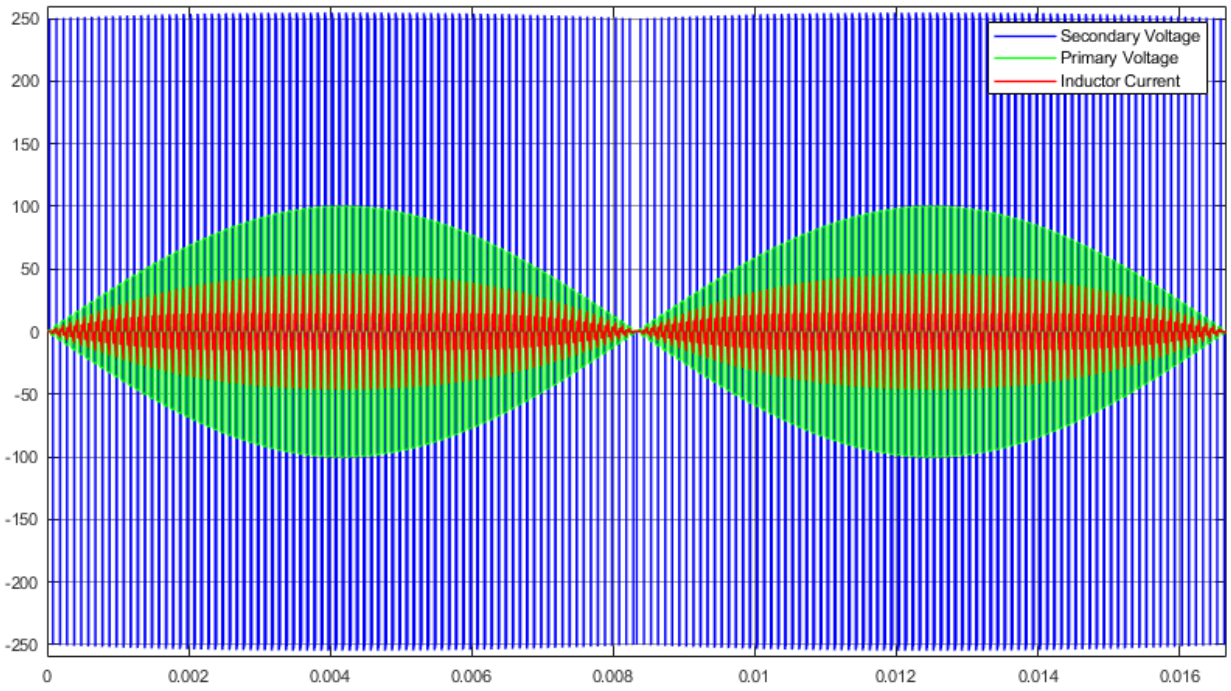

(a) One single input cycle.

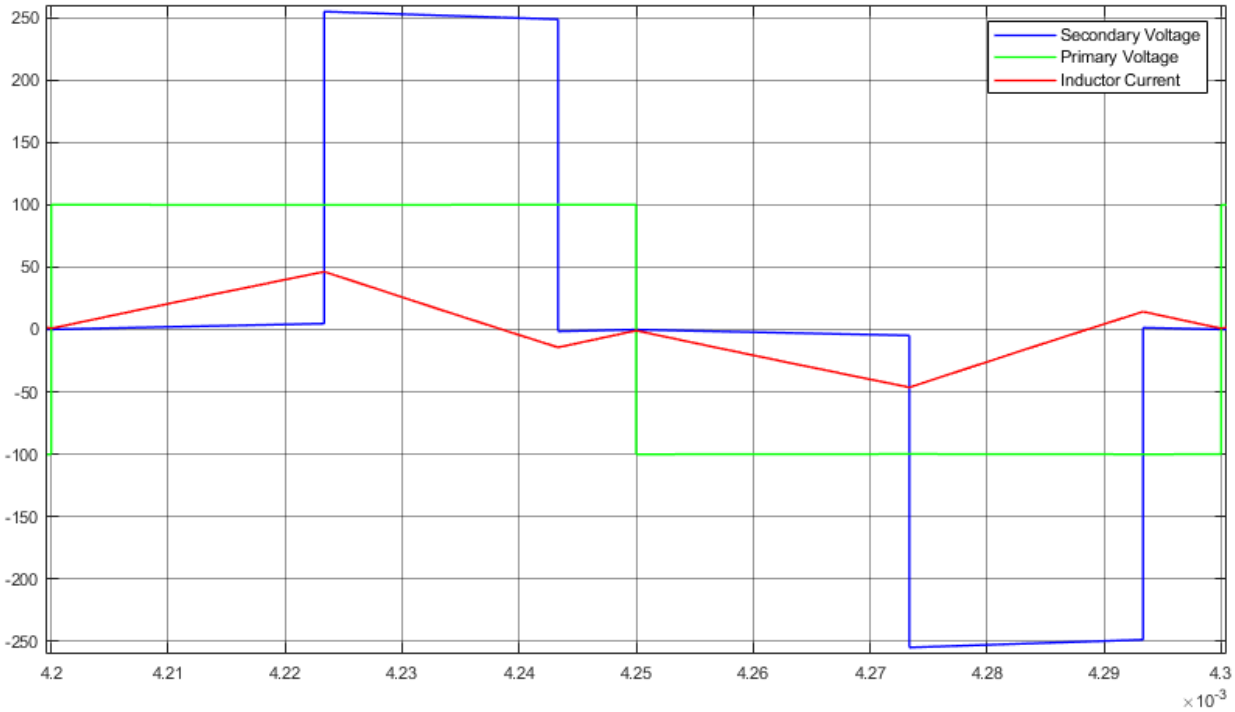

(b) Duty ratio is at its maximum.

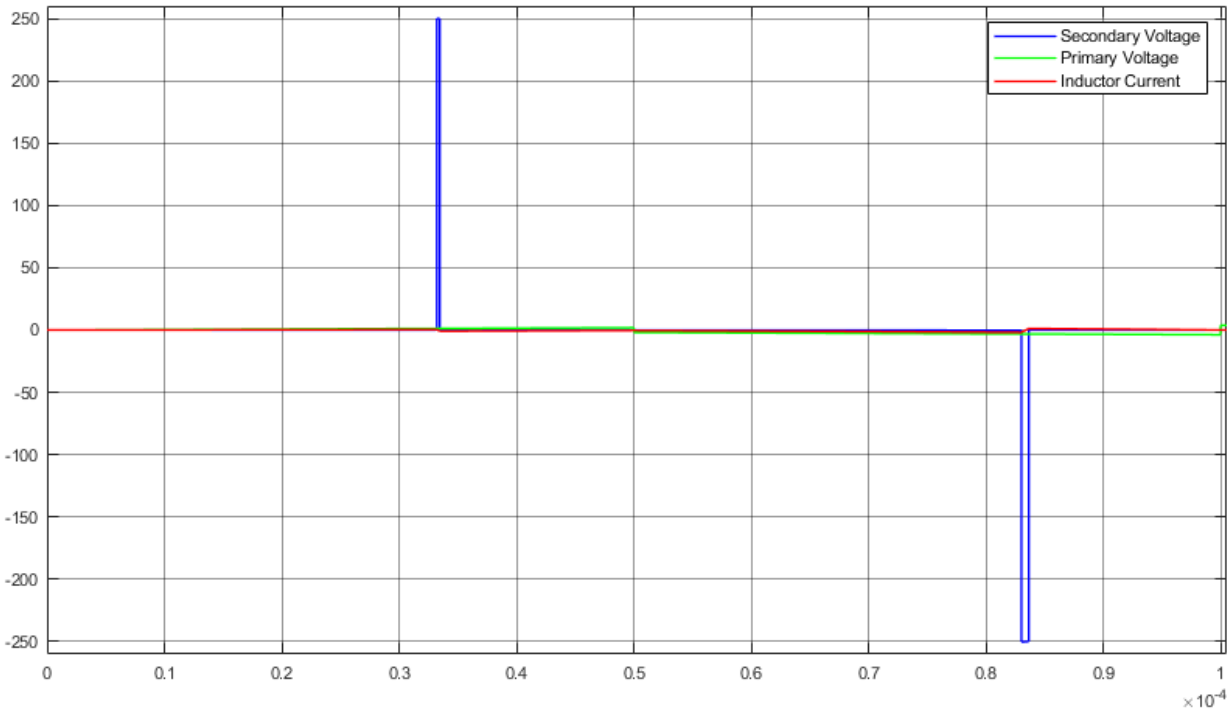

(c) Duty ratio is at its minimum.

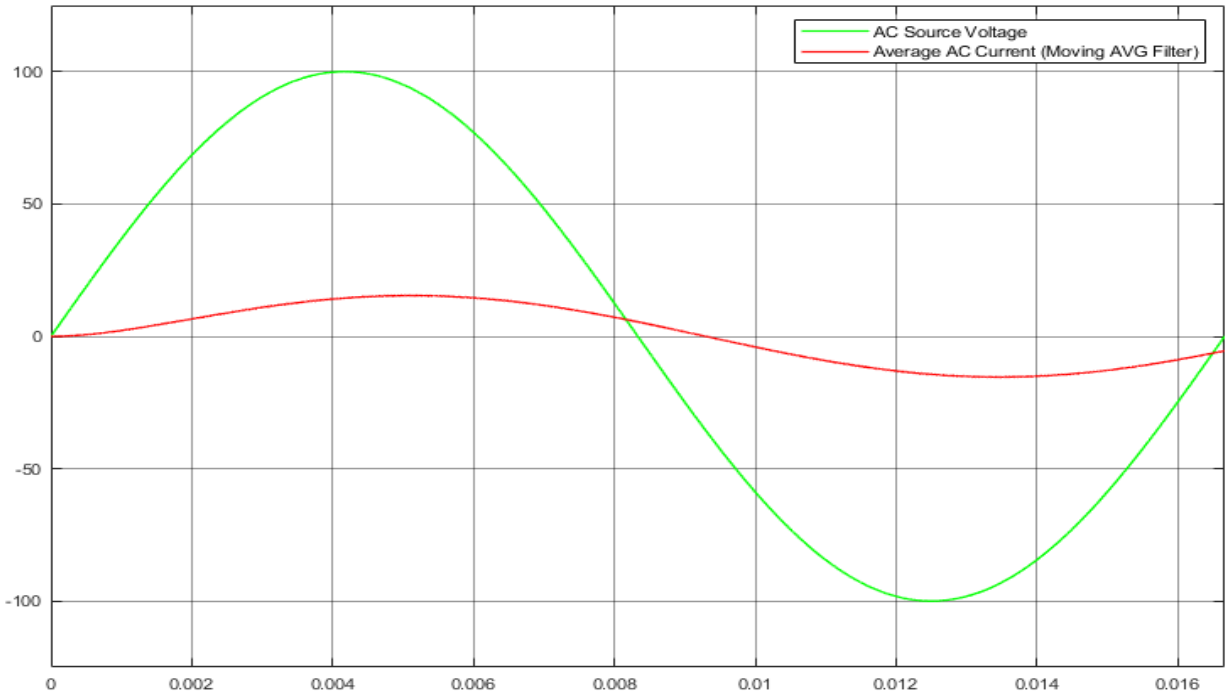

(d) Positive Power Flow.

Fig. 2.6: Simulation results when phase shift ratio is positive (+0.3).

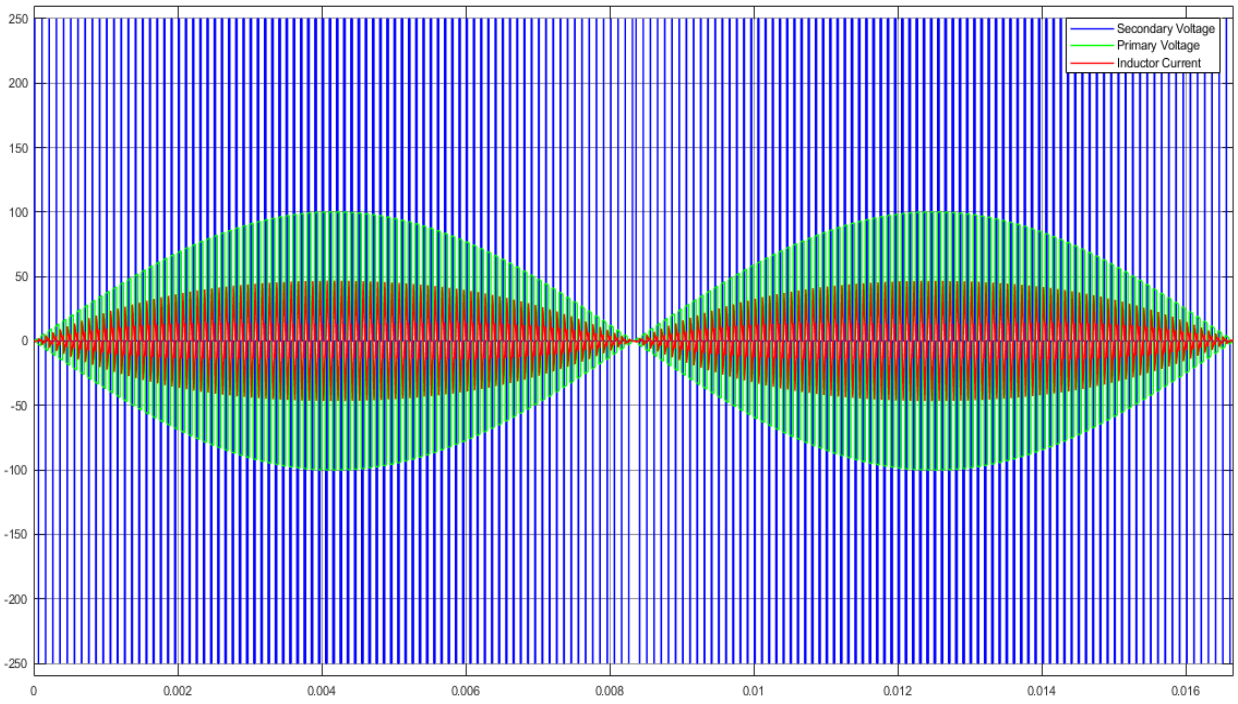

(a) One single input cycle.

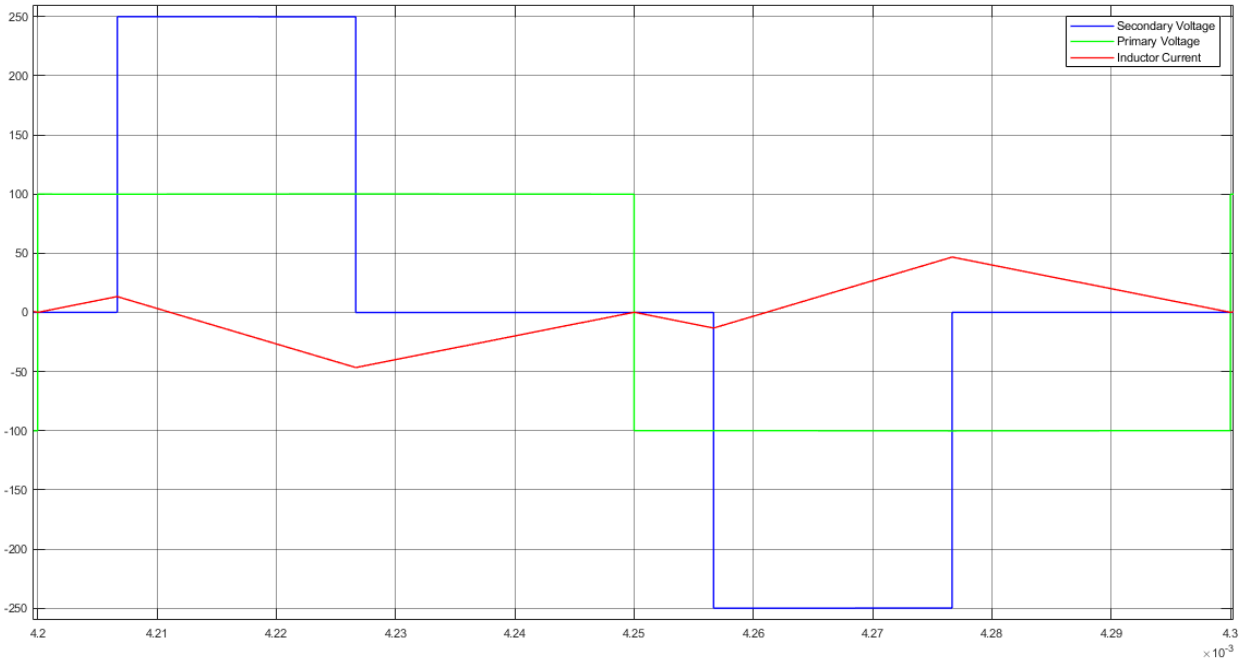

(b) Duty ratio is at its maximum.

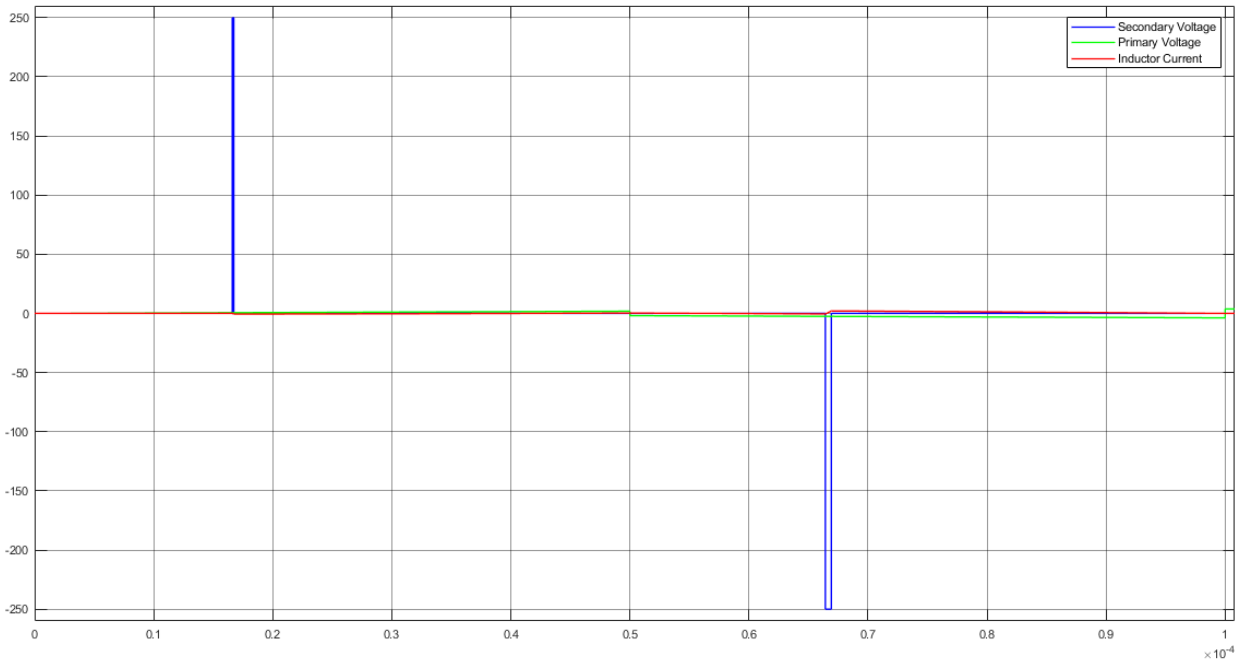

(c) Duty ratio is at its minimum.

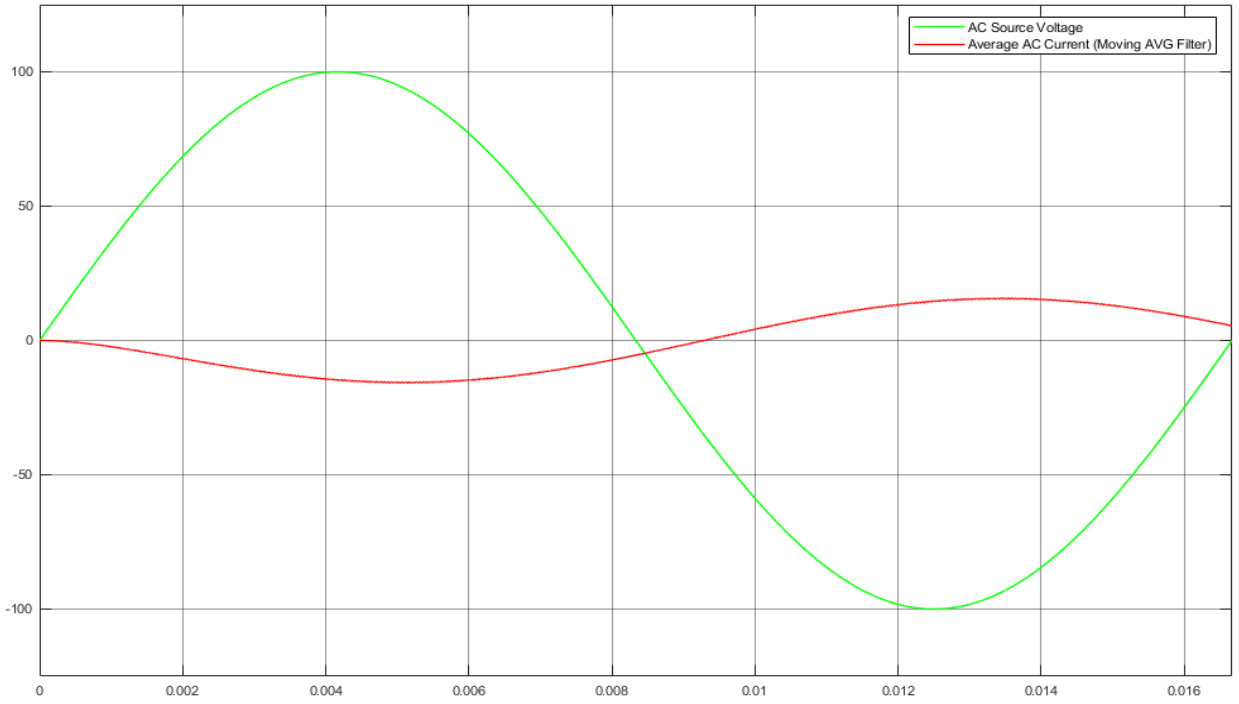

(d) Negative Power Flow.

Fig. 2.7: Simulation results when phase shift ratio is positive (+0.3).

2.3 Conclusion

The proposed single-stage DAB bi-directional AC/DC converter was analyzed in detail and simulated. The simulation results confirm the theoretical analysis. Finally, the capability of bi-directional power flow was demonstrated.

Chapter 3

Small-signal System Model Analysis

3.1 Analysis

In this chapter, a state-space averaging technique and small-signal modeling is introduced and applied to the proposed converter shown in Fig. 2.1. In the past, for modeling the switching converters in general, there were two main techniques: state-space modeling technique and averaging technique. R.D. Middlebrook and Slobodan Cuk in the literature [15] first introduced a state-space averaging method bridging the gap between the two techniques, since then this method has been generally used in power electronics. The proposed converter is controlled via the time-varying duty ratio of the gate signals and changes to phase shift ratio δ. Thus, the converter is highly non-linear having both analogue and digital features. As a result, the state-space averaging technique can be applied to linearize this system and obtain the dynamic model of the converter. See [9], [13], [14], [15], [16], [17], and [18]. The total number of storage elements in the converter determines the order of the system. In the proposed converter, one inductor is connected to the

secondary side of the transformer. Thus, this is a 1st order system. Equation (2.7) defines the inductor voltage, $v_L(t)$, for each time interval of one complete switching period, T_s. The waveform of inductor current (orange line) in Fig. 2.4 shows that the waveform during the first half switching period, whose time interval is zero to $\frac{T_s}{2}$ is asymmetric to the waveform during the second half switching period, whose time interval is time from $\frac{T_s}{2}$ to T_s because of the switching states described in Fig. 2.2 and 2.3. In other words, the total sum of the inductor current during every single complete switching period results in zero.

Thus, in using the small signal modeling process combined with the state-space averaging technique, only one variable half switching period is considered, when the switches S_1 and S_4 are on and S_2 and S_3 are off and with time varying duty ratio, *D*, and with $v_i(t) > 0$.

$$L\frac{di_L(t)}{dt} = \begin{cases} nv_i(t) - i_L R; \ 0 \le t < \frac{T_s}{4}(1+\delta-D(t)) \\ nv_i(t) - V_o - i_L R; \ \frac{T_s}{4}(1+\delta-D(t)) \le t < \frac{T_s}{4}(1+\delta+D(t)). \\ nv_i(t) - i_L R; \ \frac{T_s}{4}(1+\delta+D(t)) \le t < \frac{T_s}{2} \end{cases} \quad (3.1)$$

Equation (3.1) is rewritten from Equation (2.7) only considering the first half switching period.

$$\dot{X}(t) = \begin{cases} -\frac{R}{L}X(t) + \frac{1}{L}U(t); \ 0 \le t < \frac{T_s}{4}\left(1+\delta-D(t)\right) \\ -\frac{R}{L}X(t) + \left(\frac{1}{L} - \frac{1}{L\cdot D(t)}\right)U(t); \ \frac{T_s}{4}\left(1+\delta-D(t)\right) \le t < \frac{T_s}{4}\left(1+\delta+D(t)\right). \\ -\frac{R}{L}X(t) + \frac{1}{L}U(t); \ \frac{T_s}{4}\left(1+\delta+D(t)\right) \le t < \frac{T_s}{2} \end{cases} \quad (3.2)$$

Here, $\{A_i = -\frac{R}{L};\ i = 1,2,3\}$ and $B = [B_1\ B_2\ B_3] = \left[\frac{1}{L}\ \left(\frac{1}{L} - \frac{1}{L\cdot D}\right)\ \frac{1}{L}\right]$. The state-space averaged equation provided through the conduction ratio is written as

$$\dot{X}(t) = \left[A_1\left(\frac{\left(1+\delta-D(t)\right)}{2}\right) + A_2\left(D(t)\right) + A_3\left(\frac{\left(1-\delta-D(t)\right)}{2}\right)\right]X(t)$$

$$+\left[B_1\left(\frac{\left(1+\delta-D(t)\right)}{2}\right) + B_2\left(D(t)\right) + B_3\left(\frac{\left(1-\delta-D(t)\right)}{2}\right)\right]U(t), \quad (3.3)$$

where $D(t) = \bar{D} + d(t)$, $X(t) = \bar{X} + x(t)$, and $U(t) = \bar{U} + u(t)$. The variable *d(t)* is a small signal variation of *D(t)*, and *x(t)* is a small signal variation of *X(t)*. The mean of *D*, or $\bar{D}$, can be computed as

$$\bar{D} = \frac{n \cdot V_i}{V_o \cdot \pi} \cdot \int_0^{\pi} \sin(t)\, dt = \frac{2 \cdot n \cdot V_i}{V_o \cdot \pi}.$$

The nominal *X*, or $\bar{X}$, can be computed by averaging $i_L(t)$ over a complete cycle $0 \leq t \leq T_s$. To derive the average source current, $\bar{\imath}_i(t)$, from [1], the equation is

$$\bar{\imath}_i(t) = \frac{2n}{T_s} \cdot \int_0^{\frac{T_s}{2}} i_L(\tau)\, d\tau = \gamma_1(D(t)) + \gamma_2$$

where γ_1 is a negative approximately linear function of *D* under typical converter parameters with $0 < D(t) < 1$.

The dynamics can be rewritten as

$$\dot{\bar{X}} + \dot{x}(t) = \left[A_1\left(\frac{\left(1+\delta-(\bar{D}+d(t))\right)}{2}\right) + A_2\left(\bar{D} + d(t)\right) + A_3\left(\frac{\left(1-\delta-(\bar{D}+d(t))\right)}{2}\right)\right]\left(\bar{X} + x(t)\right)$$

$$+\left[B_1\left(\frac{\left(1+\delta-(\bar{D}+d(t))\right)}{2}\right) + B_2\left(\bar{D} + d(t)\right) + B_3\left(\frac{\left(1-\delta-(\bar{D}+d(t))\right)}{2}\right)\right]\left(\bar{U} + u(t)\right).$$

After expanding and dividing the equation then neglecting the high order small signal variation, it

yields

$$\dot{x}(t) = \left[A_1\left(\frac{-d(t)}{2}\right) + A_2\big(d(t)\big) + A_3\left(\frac{-d(t)}{2}\right)\right]\bar{X}$$
$$+ \left[A_1\left(\frac{(1+\delta-\bar{D})}{2}\right) + A_2(\bar{D}) + A_3\left(\frac{(1-\delta-\bar{D})}{2}\right)\right]x(t)$$
$$+ \left[B_1\left(\frac{(1+\delta-\bar{D})}{2}\right) + B_2(\bar{D}) + B_3\left(\frac{(1-\delta-\bar{D})}{2}\right)\right]u(t)$$
$$+ \left[B_1\left(\frac{-d(t)}{2}\right) + B_2\big(d(t)\big) + B_3\left(\frac{-d(t)}{2}\right)\right]\bar{U}$$

$$= \left[A_1\left(\frac{(1+\delta-\bar{D})}{2}\right) + A_2(\bar{D}) + A_3\left(\frac{(1-\delta-\bar{D})}{2}\right)\right]x(t)$$
$$+ \left[B_1\left(\frac{(1+\delta-\bar{D})}{2}\right) + B_2(\bar{D}) + B_3\left(\frac{(1-\delta-\bar{D})}{2}\right)\right]u(t)$$
$$+ \left[\left[-\frac{A_1}{2} + A_2 - \frac{A_3}{2}\right]\bar{X} + \left[-\frac{B_1}{2} + B_2 - \frac{B_3}{2}\right]\bar{U}\right]d(t)$$

$$\equiv Ex(t) + Hu(t) + Fd(t),$$

where

$$E = \left[A_1\left(\frac{(1+\delta-\bar{D})}{2}\right) + A_2(\bar{D}) + A_3\left(\frac{(1-\delta-\bar{D})}{2}\right)\right],$$

$$H = \left[B_1\left(\frac{(1+\delta-\bar{D})}{2}\right) + B_2(\bar{D}) + B_3\left(\frac{(1-\delta-\bar{D})}{2}\right)\right],$$

$$F = \left[-\frac{A_1}{2} + A_2 - \frac{A_3}{2}\right]\bar{X} + \left[-\frac{B_1}{2} + B_2 - \frac{B_3}{2}\right]\bar{U}.$$

In short, E is the average of A_i, H is the average of B_i, and F is the difference of A_i. Therefore, the control-to-output small-signal transfer function provided through Laplace transform is

$$\frac{x(t)}{d(t)} = [sI - E]^{-1}F = \frac{adj[sI-E]}{det[sI-E]} \cdot F. \tag{3.4}$$

3.2 Simulation

In section 3.1, only first half switching period has considered for analysis. The half switching period results will be used for designing controllers in chapter 4. In this simulation part, however, first one full switching period will be considered and simulated.

Equation (3.2) is rewritten as the first full switching period:

$$\dot{X} = \begin{cases} -\frac{R}{L}X + \frac{1}{L}U, \ 0 < t < \frac{T_s}{4}(1+\delta-D) \\ -\frac{R}{L}X + \left(\frac{1}{L} - \frac{1}{L \cdot D}\right)U, \ \frac{T_s}{4}(1+\delta-D) < t < \frac{T_s}{4}(1+\delta+D) \\ -\frac{R}{L}X + \frac{1}{L}U, \ \frac{T_s}{4}(1+\delta+D) < t < \frac{T_s}{2} \\ \frac{R}{L}X - \frac{1}{L}U, \ \frac{T_s}{2} < t < \frac{T_s}{2} + \frac{T_s}{4}(1+\delta-D) \\ \frac{R}{L}X + \left(-\frac{1}{L} + \frac{1}{L \cdot D}\right)U, \ \frac{T_s}{2} + \frac{T_s}{4}(1+\delta-D) < t < \frac{T_s}{2} + \frac{T_s}{4}(1+\delta+D) \\ \frac{R}{L}X - \frac{1}{L}U, \ \frac{T_s}{2} + \frac{T_s}{4}(1+\delta+D) < t < T_s. \end{cases} \tag{3.5}$$

Using the parameters given in Table 2.1, the simplified plant is simulated with $v_i(t)$ applied over multiple cycles. The resulting plot of inductor current is shown below for the original ($X(t)$), and simplified model ($\bar{X} + x(t)$). Fig. 3.1 contains the simulation results based on the theoretical analysis regarding equation 3.5. This simulation time is from zero to one input period, i.e. T_i = 1/60 Hz = 0.0167 seconds. Thus, time-varying duty ratio, *D(t)* is used instead of the fixed peak

duty radio, *D*, at this time. To solve six differential and sequential equations, the last solution value of each equation is used as the initial condition of the next time period equation. Here, the initial condition of the first equation of the first simulation is set to zero. The trajectory results are combined into a single plot.

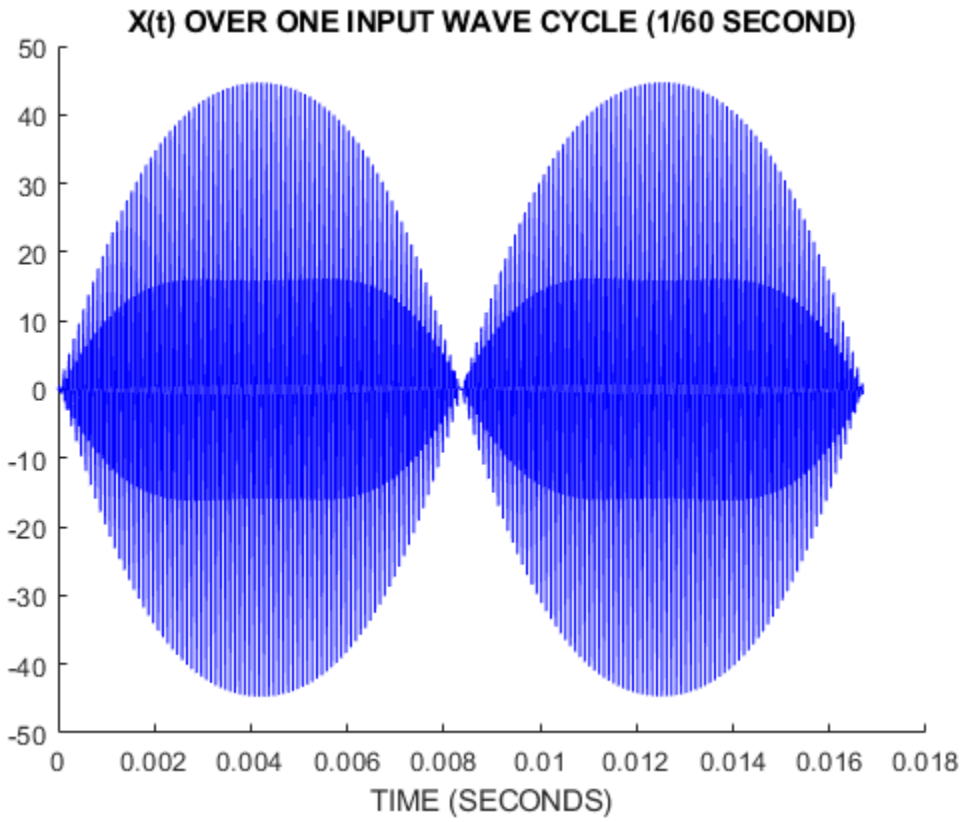

Fig. 3.1: Plot of *X(t)* over a single input waveform cycle.

During the first half of the input waveform cycle in Fig. 3.1, when the time axis is restricted to the interval [4.2e-3, 4.3e-3], i.e. the 43rd switching period, *X(t)* shows the peak amplitude of approximately 45. At this period, the time-varying duty ratio, *D(t)* is also at its maximum. Thus, the plot in Fig. 3.2 follows the plot of inductor current (orange line) in Fig. 4. Both Fig. 3.1 and 3.2 show that the inductor current has both positive and negative values.

When the only positive primary voltage, $+v_p(t)$, is applied to the inductor though the two four-quadrant switches S_1 and S_4, the inductor current increases. Here, the initial inductor current is zero. When the only negative primary voltage, $-v_p(t)$, is applied to the inductor though switches S_2 and S_3, the inductor current decreases. When both the positive primary and secondary voltages apply to the inductor, the inductor current decreases. Also, when both the negative primary and secondary voltages apply to the inductor, the inductor current increases.

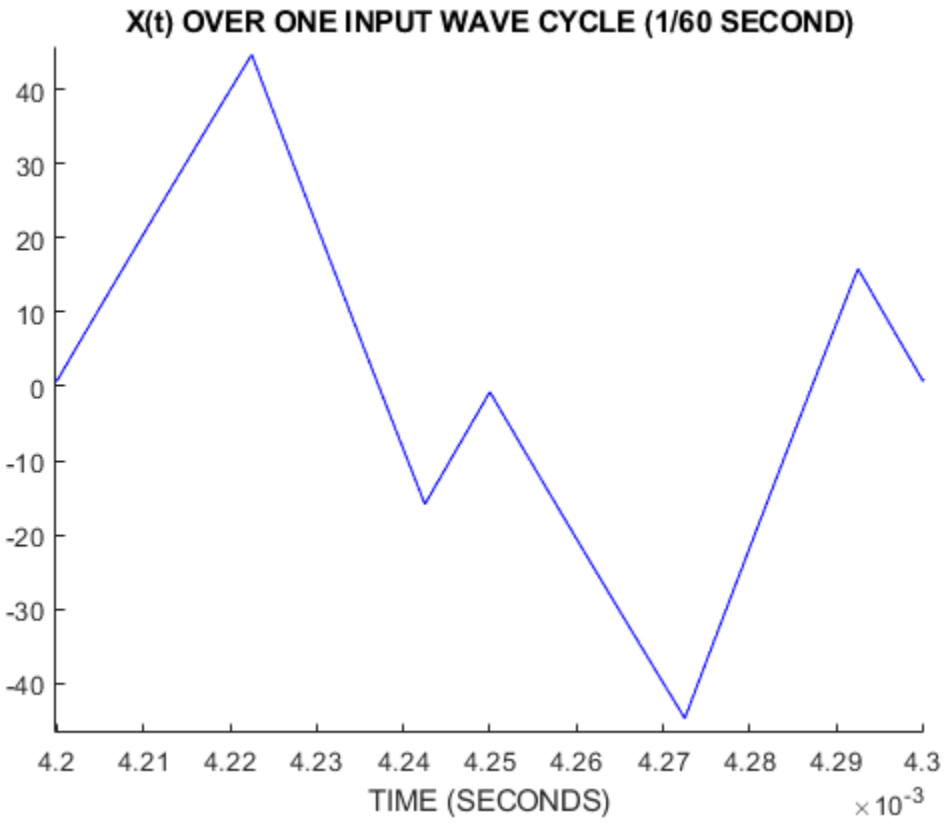

Fig. 3.2: Plot of *X(t)* over a single switching period.

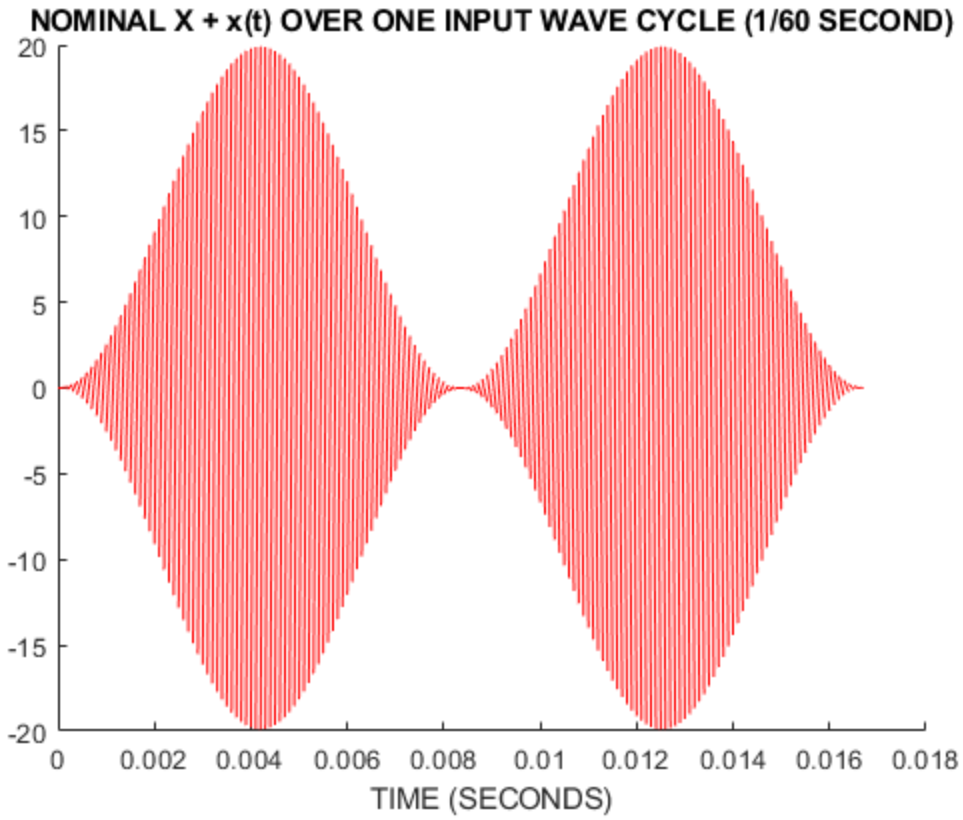

Fig. 3.3: Plot of $\bar{X} + x(t)$ over a single input waveform cycle.

Fig. 3.3 shows the simplified model by using state-space averaging technique. For time-varying condition, $D(t) = \bar{D} + d(t)$ and $X(t) = \bar{X} + x(t)$ are defined. Here, $\bar{D}$ and $\bar{X}$ are calculated as the fixed nominal values for time from zero to one input period, 0.0167 seconds. The equations for $\bar{D}$ and $\bar{X}$ are discussed on chapter 3. The parameter $x(t)$ can be derived as $x(t) = \bar{X} - X(t)$ and $d(t)$ can be derived as $d(t) = \bar{D} - D(t)$. Looking at Fig. 3.3, thick central lines are prominent with respect to the lighter peripheral lines. Thus, the peak amplitudes of the plot in Fig. 3.3 have magnitude near 20. Given that the averaged dynamics are sufficient in the modeling effort to represent the converter, the averaged model is computationally easier to implement but still captures the relevant dynamics.

3.3 Conclusion

A small signal model averaging method has been proposed to simplify the modeling dynamics of an AC/DC bi-directional DAB converter intended for grid connect applications. The proposed converter topology incorporates inductor and resistor lumped components for enhanced model accuracy and the system model was simulated (using MATLAB/Simulink) under the original exponential dynamics as well as the averaged dynamics. These simulation results were compared and demonstrate a model complexity as well as simulation computational complexity advantage for the model derived through the small signal averaged methodology.

Chapter 4

Robust Control Analysis

4.1 Analysis

There are many reference papers which cover techniques for robust control theory, especially for the H_∞ control method. These techniques are frequently implemented in high-level mathematics. It may cause some difficulties to understand even basic mechanisms of this theory. To provide appropriate context, basic control theory is briefly reviewed to justify why robust control theory is needed and to introduce the definition of robust control.

According to the reference paper in [8], historically, control theory can be broken down into two main fields: conventional control and modern control. Conventional control theory has allowed people to control the systems for centuries and became interesting with the development of feedback theory. Feedback loops can be applied to the open-loop systems, also called plants, for the purpose of stabilizing the entire system. This applied feedback system is also referred to as the

closed-loop systems.

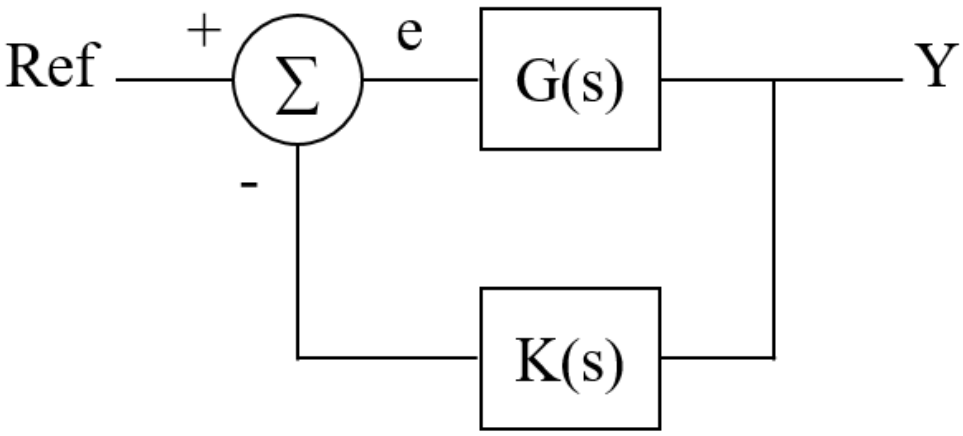

Fig. 4.1: Simple Closed-loop Control System.

Fig. 4.1 shows a simple closed-loop control system. The input to the system is a reference signal, which represents the desired control value. This reference signal is fed though a plant, having transfer function G(s), to determine the output Y. This output is fed back through a controller, having transfer function K(s). Then the controlled feedback signal is subtracted from the reference signal to determine the error signal, e. Finally, the plant dynamics are measured yielding an output which is in turn used to drive the system toward a desired reference signal.

Laplace transforms are used to express the system model equations in the frequency domain. Due to the mathematical complexity, conventional control theory historically has been used mostly for Single-Input-Single-Output (SISO) systems. In the frequency domain, G(s) and K(s) were expressed as ratios of polynomials in the complex frequency variable, s. The roots of the denominator, also referred to as poles, determine the stability of the system. The location of these poles had to be in the left half-plane of the complex frequency plot to guarantee stability. Movement of these poles into the right-half plane causes unstable systems. Nyquist, Bode, and

Root locus methods were developed to show graphically the movements of poles in the frequency domain.

Modern control theory was developed along with fast growing computer technology. The system model equations were calculated efficiently and quickly on computers. It allows for computationally feasible Multiple-Input-Multiple-Output (MIMO) systems. It was shown that any n-th order differential equations describing a system model could be reduced to multiple 1st order equations grouped in the form of a matrix. The state space matrix equations are shown:

$$\dot{\boldsymbol{x}} = A\boldsymbol{x} + B\boldsymbol{u}$$

$$\mathbf{y} = C\boldsymbol{x} + D\boldsymbol{u},$$

where $\boldsymbol{x}$ is a vector representing states, $\boldsymbol{u}$ is a vector representing inputs, and A, B, C, D are constant matrices for linear time-invariant systems. The key issue driving the need for modern control theory is optimization. Thus, many methods to optimize the constant state matrices were developed.

However, the conventional and modern control theory incorporating optimization were not always tolerant to changes inside or outside of the system [8]. Thus, robust control theory was developed because this theory can accommodate uncertainties which arise at every point of the system. In other words, the key issue with robust control systems is uncertainty and how the control system can deal with this problem. To handle uncertainties, having an appropriate model of uncertainty models is the first step. One traditional method to define an uncertainty is modeled as probability distributions via stochastic control theory. But this method has not been widely used in engineering. Robust control theory seeks to bound the uncertainty rather than express it in a direct distribution

form. Given a bound on the uncertainty, the controller can deliver results that meet the system requirements in all cases. Therefore, robust control theory can be stated as a worst-case analysis method.

Due to the inconsistent nature of wind and solar by time-varying climate condition, the PV panels and wind turbines may generate unpredictable power. Also, the system of renewable energy sources itself may not operate properly if subsystem components are worn-out or broken. All assumptions above can be considered as uncertainties. According to [21] and [22], among the robust control techniques that are being gradually investigated in power electronics, the H_∞ approach is a good candidate in many applications due in part to its linear characteristics, and the derived controller which can also be used in large signal applications such as wind turbine generators. The main antecedent in the use of H_∞ control in DC-DC boost converters can be found in the paper of Naim *et al*. [20]. According to this literature, the conventional closed-loop control approach to DC-DC switch-mode converter shows a major problem when the transfer function from the control input to the output voltage has a right-half-plane-zero (RHPZ). In conventional design, designing low-output impedance (minimized weighting function) is not an objective. Rather, it is obtained indirectly by increasing the loop gain and this increase is generally in conflict with the phase-margin requirement. Thus, the presence of an RHPZ severely restricts the closed-loop bandwidth. However, the goal H_∞ control strategy is to design the minimized output impedance as much as possible over a given frequency range and this can be overcome the difficulties of the conventional approach.

Regarding the application of H_∞ robust control techniques to the power electronic converters application, most of papers were published for DC-DC buck, boost or buck-boost converter in [10],

[19], [20], [21], [22], [23], [24], [25], and [26]. However, in this thesis, H_∞ robust controller for AC-DC bi-directional DAB converter is investigated.

In the H_∞ approach, the infinity norm, denoted as $\|\cdot\|_\infty$, of each input/output signal has upper bound of unity.

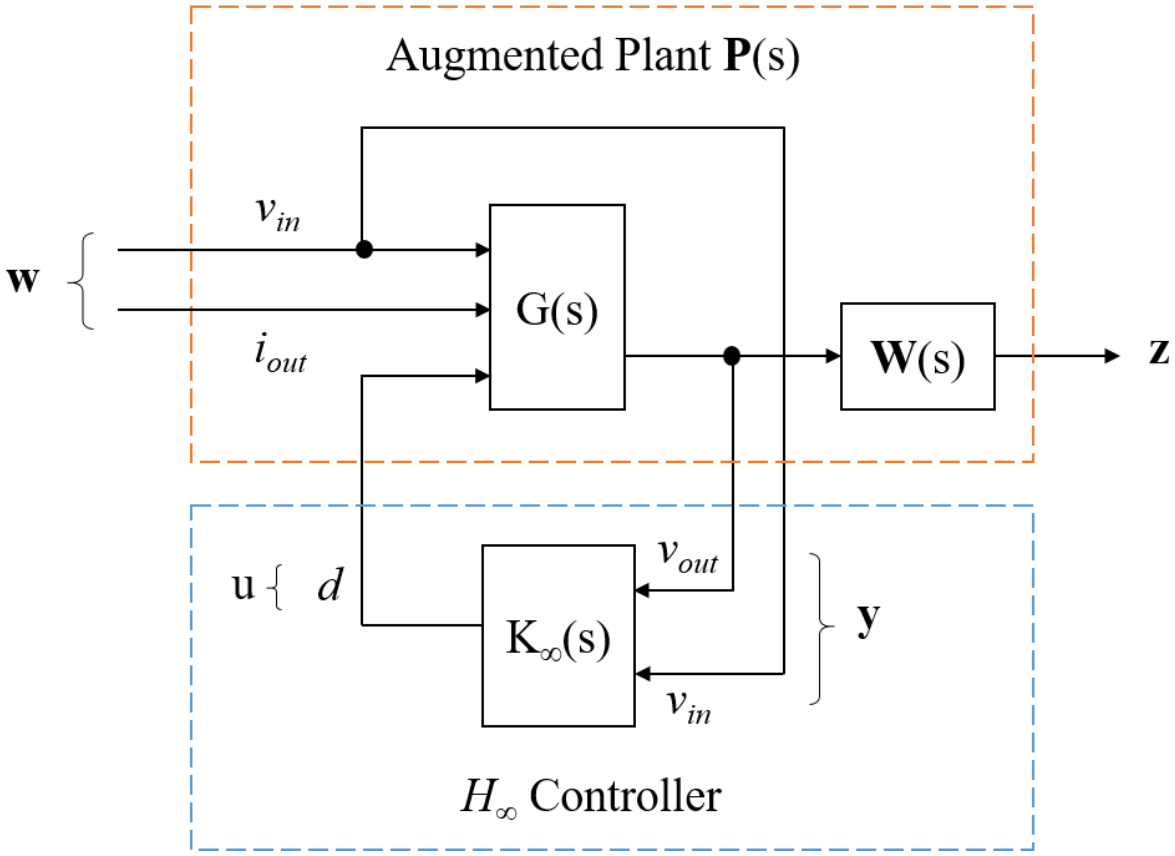

(a) General H_∞ Control Representation for the Converter

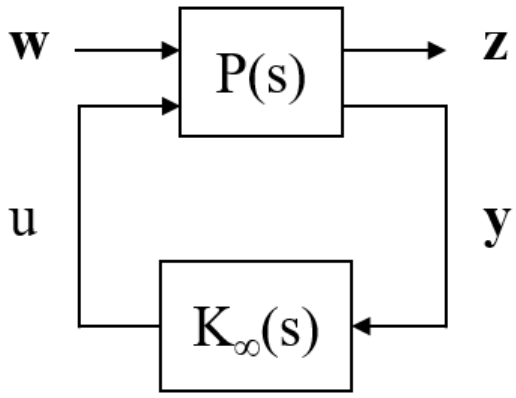

(a) Compact H_∞ Control Representation.

Fig. 4.2: H_∞ Controller Design for the Converter.

General H_∞ control representation for the converter in Fig. 4.2 (a) from [20] and [31] shows the converter model (G(s)), the H_∞ controller ($K_\infty(s)$), and the stable vector weighting function (**W**(s)). The vector **w** contains the perturbations (v_{in} and i_{out}), the output vector **z** is the weighted error signal, the vector **y** contains the measurement outputs of the converter (v_{out} and v_{in}), and the control input u is the duty cycle (d).

The simplified H_∞ control representation is showed in Fig. 4.2 (b) from [21] and [26], where **P**(s) is the augmented plant.

Assuming that **x** is the state vector of the plant, **w** is the input of the plant, **y** is the input of the H_∞ controller, and **u** is the output of the H_∞ controller, the state space system equations for general plant (but not related to the converter application) is described as follows:

$$\dot{\mathbf{x}} = \mathrm{A}\mathbf{x} + \mathrm{B}_1\mathbf{w} + \mathrm{B}_2\mathbf{u}$$

$$\mathbf{z} = \mathrm{C}_1\mathbf{x} + \mathrm{D}_{11}\mathbf{w} + \mathrm{D}_{12}\mathbf{u}$$

$$\mathbf{y} = \mathrm{C}_2\mathbf{x} + \mathrm{D}_{21}\mathbf{w} + \mathrm{D}_{22}\mathbf{u}$$

$$\mathbf{u} = \mathrm{K}_{\infty}(\mathrm{s}) \cdot \mathbf{y}.$$

P(s) is the general plant which can be described in matrix form as

$$\mathbf{P}(\mathrm{s}) = \begin{bmatrix} \mathbf{A}_{\mathrm{P}} & \mathbf{B}_{\mathrm{P}} \\ \mathbf{C}_{\mathrm{P}} & \mathbf{D}_{\mathrm{P}} \end{bmatrix}.$$

Linear fractional transformation (LFT) is described in K. Zhou et al. [27] and it used to get a transfer function using above equations.

According to the reference paper [21], the closed-loop transfer function matrix, $\boldsymbol{T_{zw}}$, can be obtained using LFT as below:

$$\mathbf{T_{zw}} = \frac{\mathbf{z}}{\mathbf{w}} = [\mathbf{A}_{\mathrm{P}} + \mathbf{B}_{\mathrm{P}} \cdot \mathrm{K}_{\infty}(\mathrm{s}) \cdot (\mathbf{I} - \mathbf{D}_{\mathrm{P}} \cdot \mathrm{K}_{\infty}(\mathrm{s}))^{-1} \cdot \mathbf{C}_{\mathrm{P}}],$$

where,

$$\mathbf{A}_{\mathrm{p}} = \mathrm{A},\ \mathbf{B}_{\mathrm{p}} = [\mathrm{B}_1 \quad \mathrm{B}_2],\ \mathbf{C}_{\mathrm{p}} = \begin{bmatrix} \mathrm{C}_1 \\ \mathrm{C}_2 \end{bmatrix},\ \mathbf{D}_{\mathrm{p}} = \begin{bmatrix} \mathrm{D}_{11} & \mathrm{D}_{12} \\ \mathrm{D}_{21} & \mathrm{D}_{22} \end{bmatrix},$$

and **I** is the identity matrix of appropriate dimension.

The goal of H_{∞} control is to find a controller $\mathrm{K}_{\infty}(\mathrm{s})$ that stabilizes the plant **P**(s) minimizing the ∞-norm of $\mathbf{T_{zw}}$.

And the transfer function matrix, $\mathbf{T_{zw}}$, can be describes as below:

$$||\mathbf{T_{zw}}||_{\infty} = sup\ \bar{\sigma}(w) < \gamma, \qquad 0 < \gamma \leq 1$$

where $||\mathbf{T_{zw}}||_{\infty}$ is the maximal gain of the transfer function matrix $\mathbf{T_{zw}}$, here, $\|\cdot\|_{\infty}$ denotes the matrix which is the supremum (sup) of the $\mathbf{T_{zw}}$ over all frequencies, and $\bar{\sigma}(w)$ is a maximum singular value. For more mathematical descriptions, see [20], [21], [26].

In practice, an H_∞ controller with $||\mathbf{T_{zw}}||_\infty$ as close to $\gamma_{optimal}$ can be obtained by the Robust Control Toolbox of MATLAB, called *hinfsyn* function. This function needs only the state-space description of the plant (the state-space averaged converter model from chapter 4) and stable weighting functions for uncertainty.

4.2 Simulation

Applying the transfer function of the proposed converter by the state-spacing averaged technique, equation (3.4), and selecting the weighting functions for uncertainty models, optimal H_∞ controller can be designed using *hinfsyn* function in MATLAB.

The linearized converter's transfer function G can be rewritten as below by using equation (3.4) and Table 2.1:

$$\mathrm{G(s)} = \frac{x}{d}(\mathrm{s}) = \frac{\hat{\imath}_L}{d}(\mathrm{s}) = \frac{-50000}{s+2000}\mathrm{U} \tag{4.1}$$

A MATLAB function, *augw*, can build a state-space model of an augmented LTI plant **P**(s) with three weighting functions $W_1(s)$, $W_2(s)$, and $W_3(s)$ indicating uncertainty to the error signal, control signal, and output signal respectively. Fig. 4.3 shows the block diagram of *augw* function.

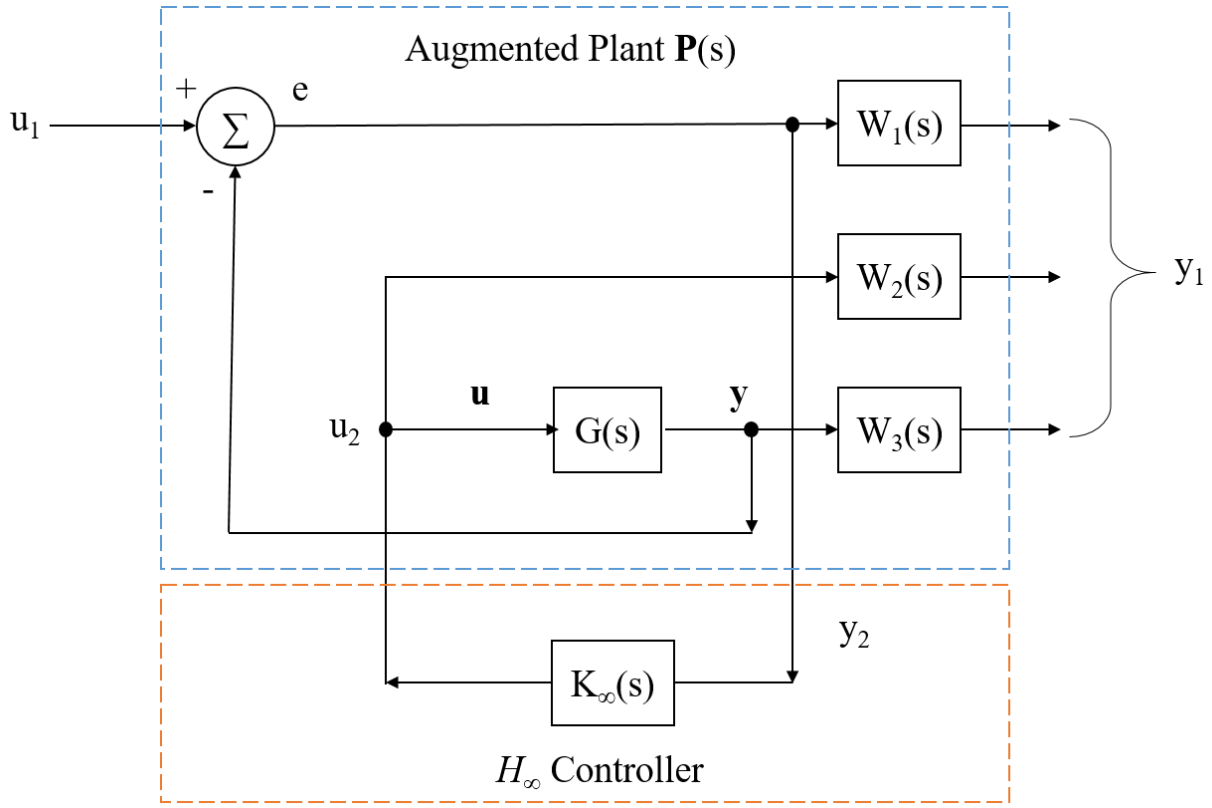

Fig. 4.3: Block Diagram of *augw* Function in MATLAB.

And the three stable weighting functions showing all negative poles, for uncertainty model were chosen as:

$$W_1(s) = \frac{0.1 \cdot (s + 10)}{10s + 1}$$

$$W_2(s) = \frac{-0.1 \cdot (s + 1000)}{1000s + 1}$$

$$W_3(s) = \frac{0.1 \cdot (s + 1000)}{1000s + 1}$$

Combining the converter transfer function (G(s)) with the three weighting functions ($W_1(s)$, $W_2(s)$, and $W_3(s)$), the transfer function of H_∞ controller, $K_\infty(s)$, is calculated in MATLAB as:

$$K_\infty(s) = \frac{-73.17s^3 - 1.463 \cdot 10^5 s^2 - 292.7s - 0.1463}{s^4 + 5.001 \cdot 10^6 s^3 + 6.756 \cdot 10^6 s^2 + 6.773 \cdot 10^6 s + 6706}$$

Here, the widely used PI controller and proposed H_∞ controller are applied to the converter system separately and compared.

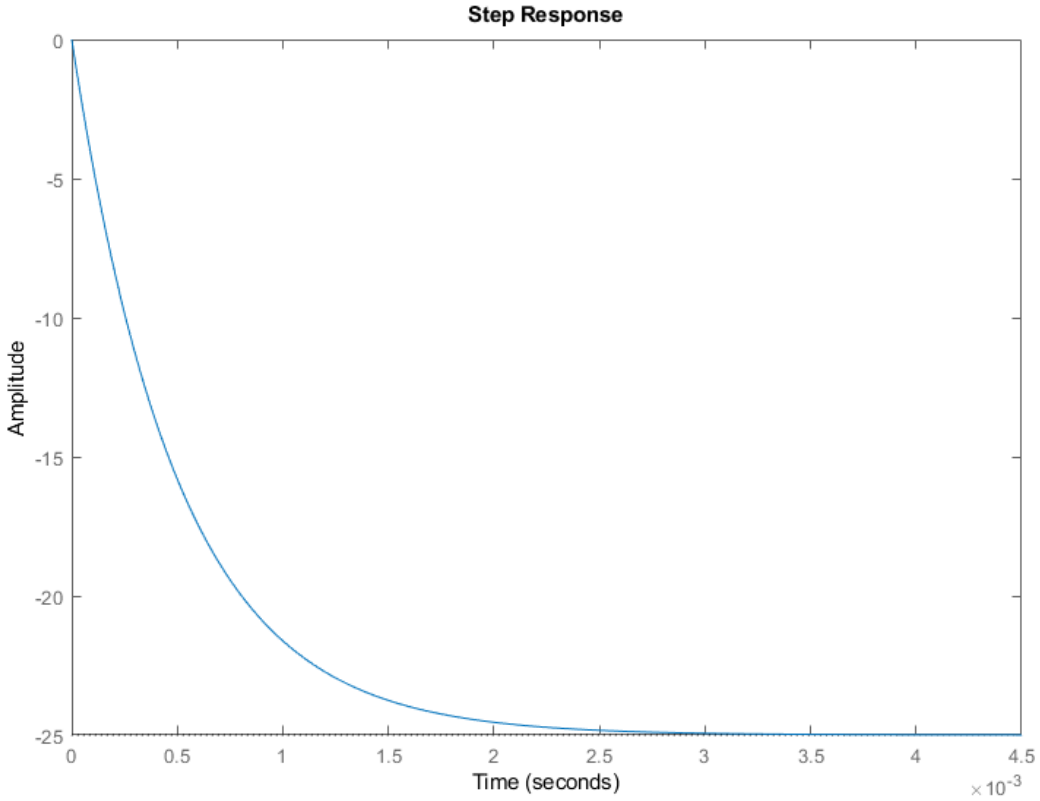

Fig. 4.4: Step Response of G(s).

In Fig. 4.4, the DC gain of the proposed converter is -25 and it is the final value of the output to a unit step input. The (negative) rise time is about 1 ms and the settling time is about 1.5 ms. PI controller tends to decrease the rise time, increase overshoot and reduce the steady-state error. MATLAB provides a tool, *pidTuner*, for automatically choosing optimal PID gains to balance performance (response time, bandwidth) and robustness (stability margins), avoiding the trial and

error process of traditional PID tuning method.

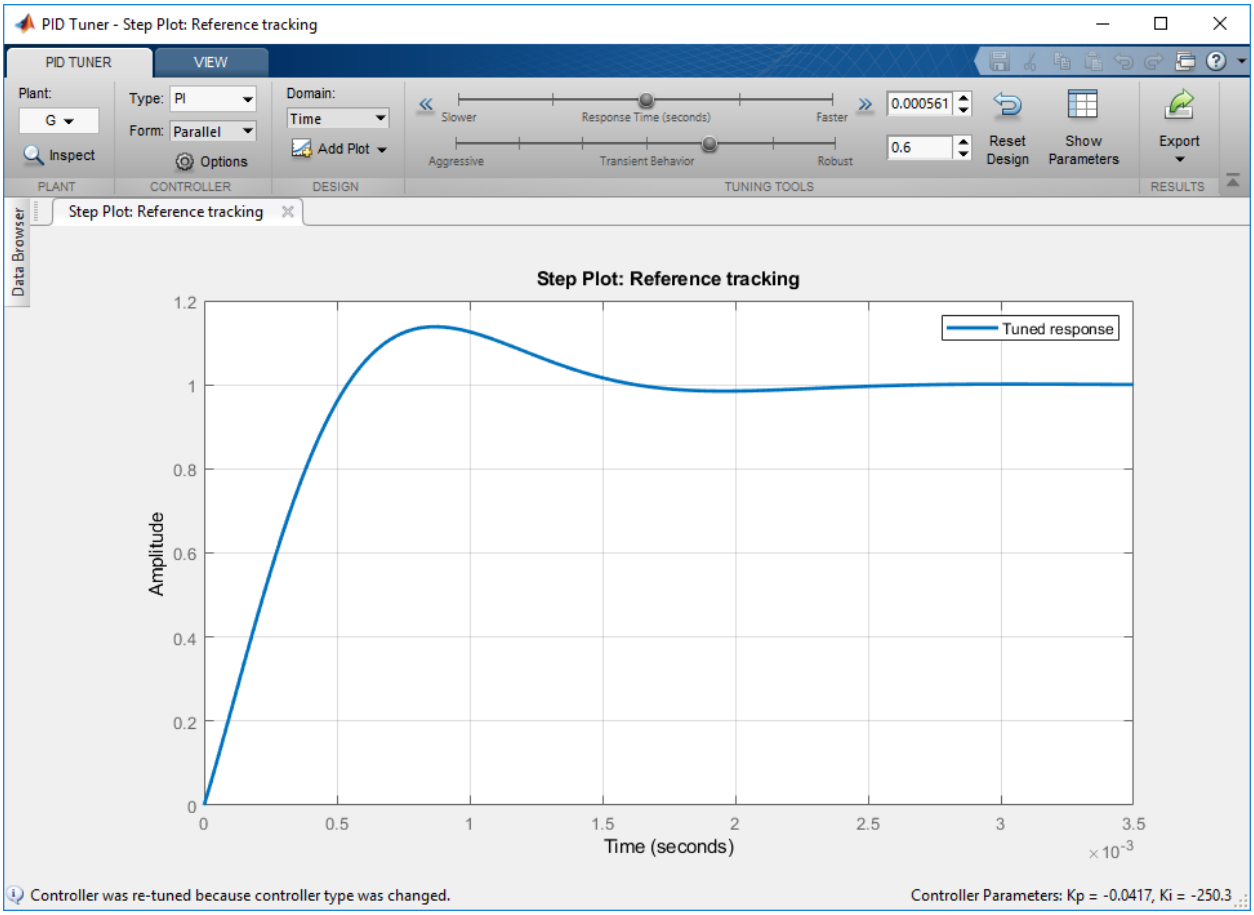

Fig. 4.5: Step Response of G(s) Applied by PI Controller.

According to Fig 4.5 and 4.6, the tuned parameters for PI controller. K_p is -0.0417 and K_i is -250.3. Rise time is 0.405 ms, settling time is 1.48 ms, and overshoot is 13.8%. It also shows the closed-loop stability is stable.

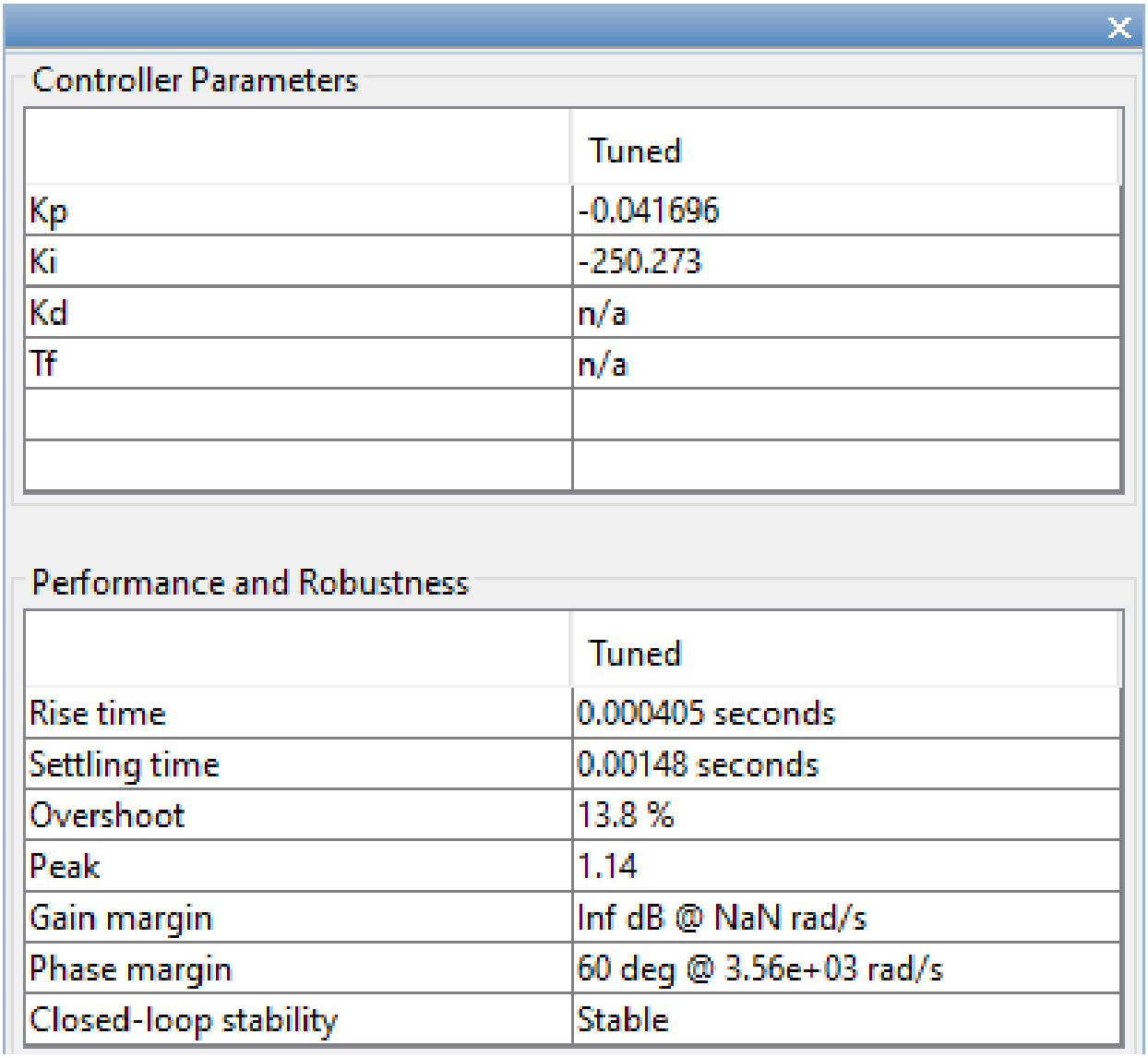

Controller Parameters

	Tuned
Kp	-0.041696
Ki	-250.273
Kd	n/a
Tf	n/a

Performance and Robustness

	Tuned
Rise time	0.000405 seconds
Settling time	0.00148 seconds
Overshoot	13.8 %
Peak	1.14
Gain margin	Inf dB @ NaN rad/s
Phase margin	60 deg @ 3.56e+03 rad/s
Closed-loop stability	Stable

Fig. 4.6: Simulation results of the PI controlled converter system.

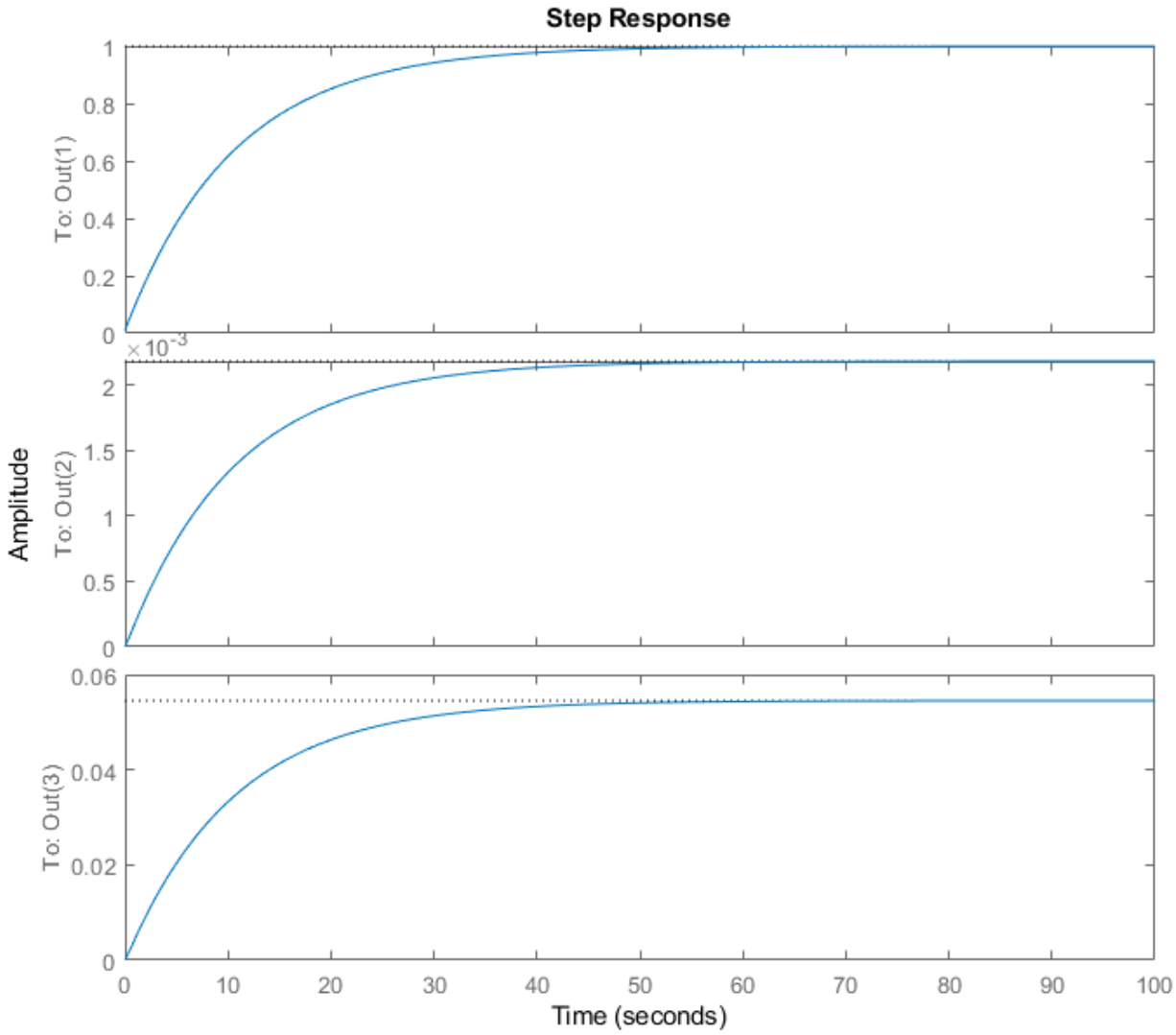

Fig. 4.7: Step Response of H_∞ Controlled Converter System.

The first plot is the simulation step response result regarding from input u_1 to output $W_1(s)$, the second plot is from u_1 to $W_2(s)$, and the third plot is from u_1 to $W_3(s)$ in Fig. 4.3. Even though all of these three results do not indicate overshoot but rise time and settling time (about 45 sec) are slower than the PI controlled system. The compared results seem to the PI controller shows better performance than the H_∞ controller. However, the given simulated conditions for both controllers are different. Regarding the PI controller, only the small-signal plant model, G(s), is considered

without weighting functions (noises or perturbations) because PID control theory and the MATLAB function, *pidtuner*, can be applied to only a SISO (Single-Input-Single-Output) system. However, the H_∞ control theory and the MATLAB function, *augw* and *hinfsyn*, must be considered the plant model with weighting functions. In other words, both controllers are not compared under the same condition due to the theoretical issue. Thus, at this moment, we cannot determine which control technique is better. And finding an optimal method to compare two control techniques under the same condition will be the future work.

4.3 Conclusion

Robust H_∞ control theory was introduced and the simulations were implemented comparing the result of H_∞ controller with PI controller to the proposed converter. According to the simulation results, even though the PI controller applied to the proposed converter looks more effective than an H_∞ controller, we could not conclude which is better controller due to different simulated conditions by different approached PID and H_∞ theories. Thus finding a method to compare two controllers will be the future work.

Chapter 5

Hybrid System Model Analysis

5.1 Analysis

Hybrid systems describe the behavior of dynamical systems that interact between continuous and discrete dynamics [16], [17]. Continuous dynamics can be typically represented by several different differential equations, or a continuous-time control system, such as a linear system $\dot{x} = Ax + Bu$, where x *is* state and u is control input. Meanwhile, discrete dynamics such as finite-state machine with state q that describe the digital or logical behavior.

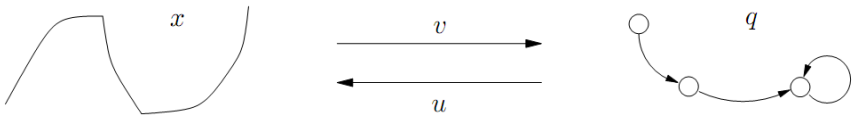

Continuous Dynamics Interaction Discrete Dynamics

Fig. 5.1: A Simple Mechanism of a Hybrid System.

Fig. 5.1 shows a brief hybrid system mechanism. A hybrid system arises when the input *v* determined by the continuous state *x* triggers the discrete dynamics or the input *u* determined by the discrete dynamics state *q* yields continuous dynamics.

Switched systems are subordinate to hybrid systems. Based on the concept of hybrid systems, greater emphasis on properties of the continuous dynamics neglecting the details of discrete dynamics but considering all possible switching patterns can be referred to as switched systems. The proposed converter has continuous-time behavior with discrete switching events. Thus, this converter can be described by the properties of switched systems. Using the stored energy in the inductor, especially inductor current, as a Lyapunov function, a switching rule is applied to the converter. Then, stability analysis and control synthesis for this switched converter system will be derived by construction of piecewise continuous Lyapunov functions.

A stable switching method by a Lyapunov function exists as long as there exists a stable convex combination of the system matrices. The switching signal may depend on time, state, or generated by more complex techniques. In this thesis, the switching signal is defined by the state (inductor current).

In this section, a pair of two unstable affine systems, A_1 and A_2, is considered. The control objective is to switch between the two systems to asymptotically stabilize the state trajectory of

$$\dot{x}(t) = A_\alpha x(t) + b_\alpha \tag{5.1}$$

by proper choice of a switching rule defined by $\alpha : \mathbb{R}^n \times \mathbb{R} \rightarrow \{1, 2\}$ which is piecewise constant, called *switching signal*, over finite intervals. The subsystem $\sum_i$ is active when $\alpha = i$, where $i = 1, 2$.

To construct Lyapunov functions for switched systems, finding a stable convex combination is the first step. To find the stable convex combination, the approach proposed by Wicks et al. [27] introduces three different methods: time average control, sliding mode control, and finite-time switched control. In this paper, only time average switching strategy will be used to define a stable convex combination.

The averaged system, also referred to as a convex combination of the subsystems, can be defined:

$$\sum_{eq} : \dot{x} = A_{eq}x + b_{eq}, \tag{5.2}$$

where $A_{eq} = \alpha A_1 + (1-\alpha)A_2 \; and \; b_{eq} = \alpha b_1 + (1-\alpha)b_2$ with $0 < \alpha < 1$. Therefore $\alpha + (1-\alpha) = 1$.

The time average control implements A_{eq} by rapid time switching between A_1 and A_2. Here, A_1 has a duty cycle proportional to α and A_2 has a duty cycle proportional to $(1-\alpha)$. Asymptotic stability requires that A_{eq} be a stability matrix and b_{eq} is zero, i.e.

$$A_{eq} = \alpha A_1 + (1-\alpha)A_2 \; is \; Hurwitz \tag{5.3}$$

$$b_{eq} = \alpha b_1 + (1-\alpha)b_2 = 0 \tag{5.4}$$

See [27] for a theorem and its proof regarding (5.3) and (5.4).

This is an algorithm for finding an α for which A_{eq} is stable according to [27]:

(i) Compute the set

$$\{\beta_i > 0 | \exists \omega_i \ni det[A_1 + \beta_i A_2 + j\omega_i I] = 0\}$$

and order this set so that $\beta_1 \leq \beta_2 \leq \cdots \leq \beta_m$ where m is the cardinality of the set.

(ii) Define the set of interval endpoints

$$B = \{0, \beta_1, \cdots, \beta_m, \infty\}$$

(iii) Define the set of test points

$$\Gamma = \left\{\gamma_0 = \frac{\beta_1}{2}, \gamma_1 = \frac{\beta_1+\beta_2}{2}, \cdots, \gamma_i = \frac{\beta_i+\beta_{i+1}}{2}, \cdots, \gamma_{m-1} = \frac{\beta_{m-1}+\beta_m}{2}, \gamma_m = 2\beta_m + 1\right\}.$$

(iv) Determine if $\Lambda[A_1 + \gamma_i A_2] \subset \mathbb{C}^-$ for some i. If so then $\alpha = \frac{1}{\gamma_i+1}$ satisfies $\lambda\left[A_{eq}(\alpha)\right] \subset \mathbb{C}^-$. Otherwise no such α exists.

Then, the α can be applied to the Lyapunov equation to find its solution, P_{eq}:

$$A_{eq}^T P_{eq} + P_{eq} A_{eq} = -Q_{eq}, \tag{5.5}$$

where Q_{eq} is any positive definite real symmetric 2x2 matrix, such as the identity matrix.

Using the solution of the Lyapunov function, Q_1 and Q_2 are calculated by the equation below:

$$Q_i = -\left(A_i^T P_{eq} + P_{eq} A_i\right), \tag{5.6}$$

where i = 1, 2.

[1] and [2] describe the switching rule based on the above results.

$$s_1(x) = x^T(Q_1 - \epsilon Q_2)x$$

$$s_2(x) = x^T(Q_2 - \epsilon Q_1)x$$

Where ϵ is any number chosen to satisfy $0 < \epsilon < 1$.

$$det[A_1 + \beta_i A_2 + j\omega_i I] = 0$$

5.2 Simulation

Parameter	Value	Unit
α	0.6	
L	50	uH
R	0.1	Ohm
ϵ	0.05	

Table 5.1: Simulation Parameters.

The input AC voltage (100 V peak; Green), output DC voltage (250 V peak; Blue), and the inductor current (Red) of the proposed AC/DC DAB converter in Fig 2.1, are simulated again in Fig 5.2 showing two and half cycles. Yellow dotted circles indicate switching points when input AC voltage swings from positive to negative or from negative to positive. Here, each switching point can be defined by two different systems. Each Fig.5.3 (a), (b), (c), and (d) is zoomed in and showed from the number 1, 2, 3, and 4 separately of Fig. 5.2.

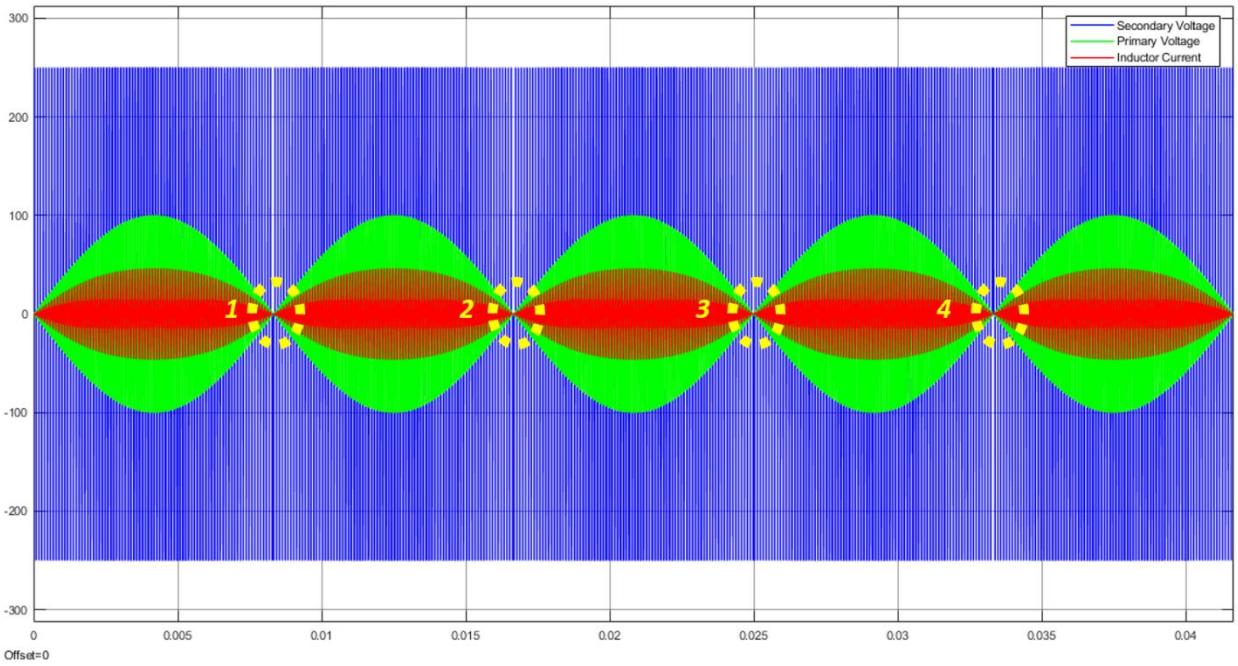

Fig. 5.2: Two and Half Cycles.

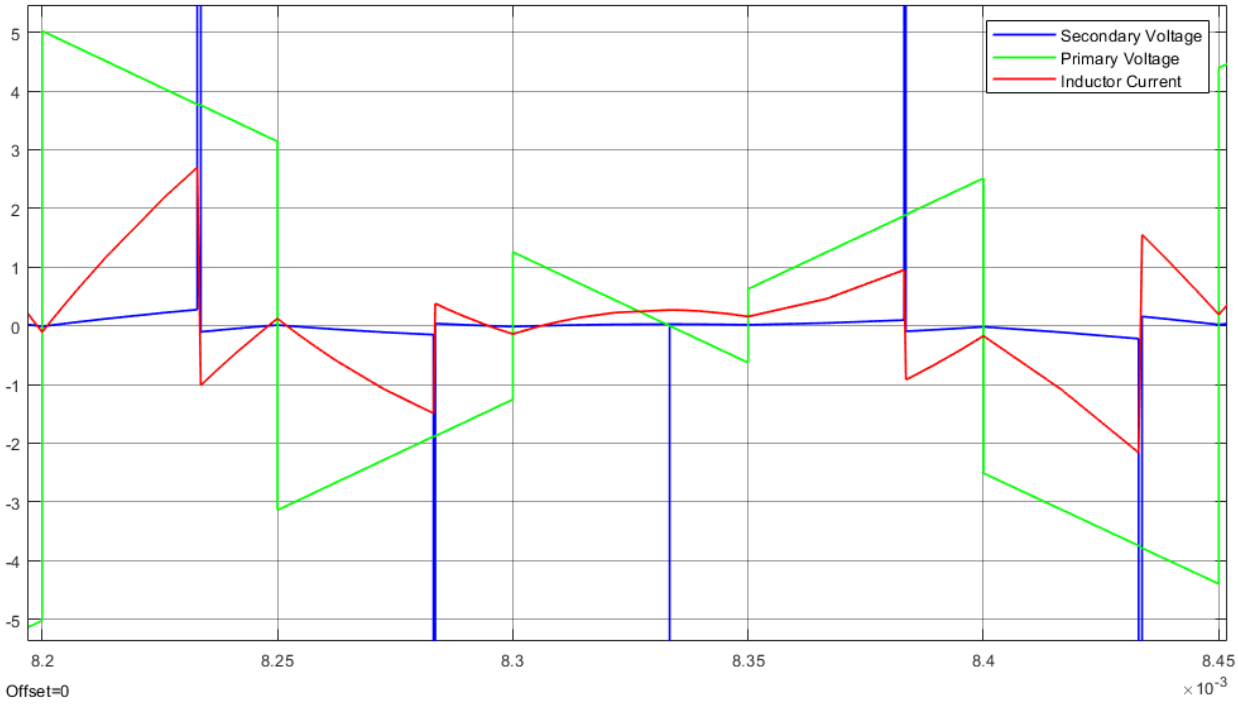

(a) First Switching Point ($t = T_i/2$).

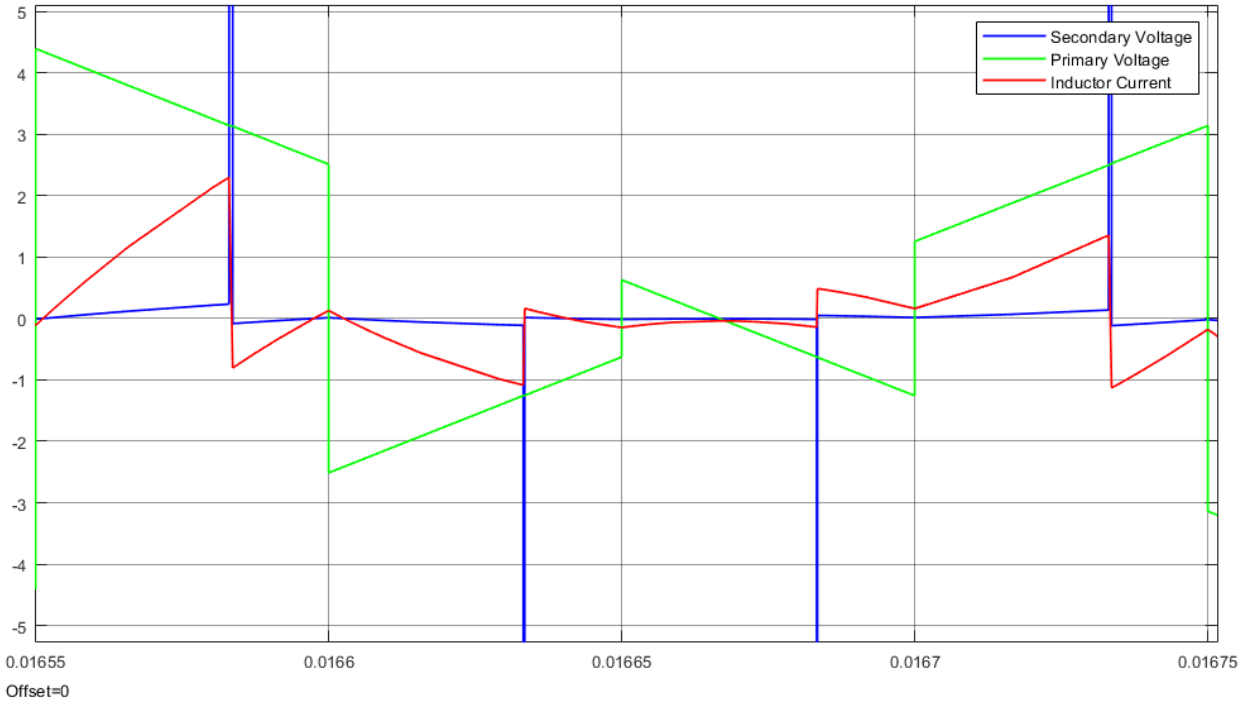

(b) Second Switching Point ($t = T_i$).

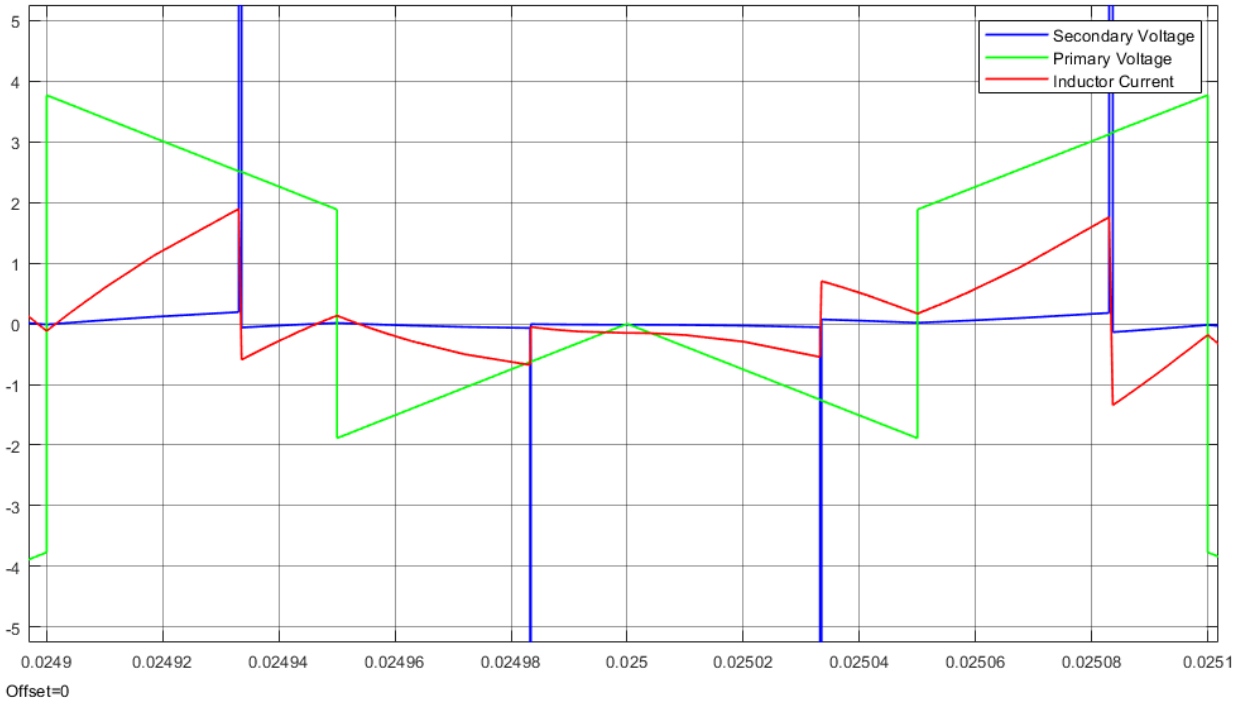

(c) Third Switching Point ($t = 3*T_i/2$).

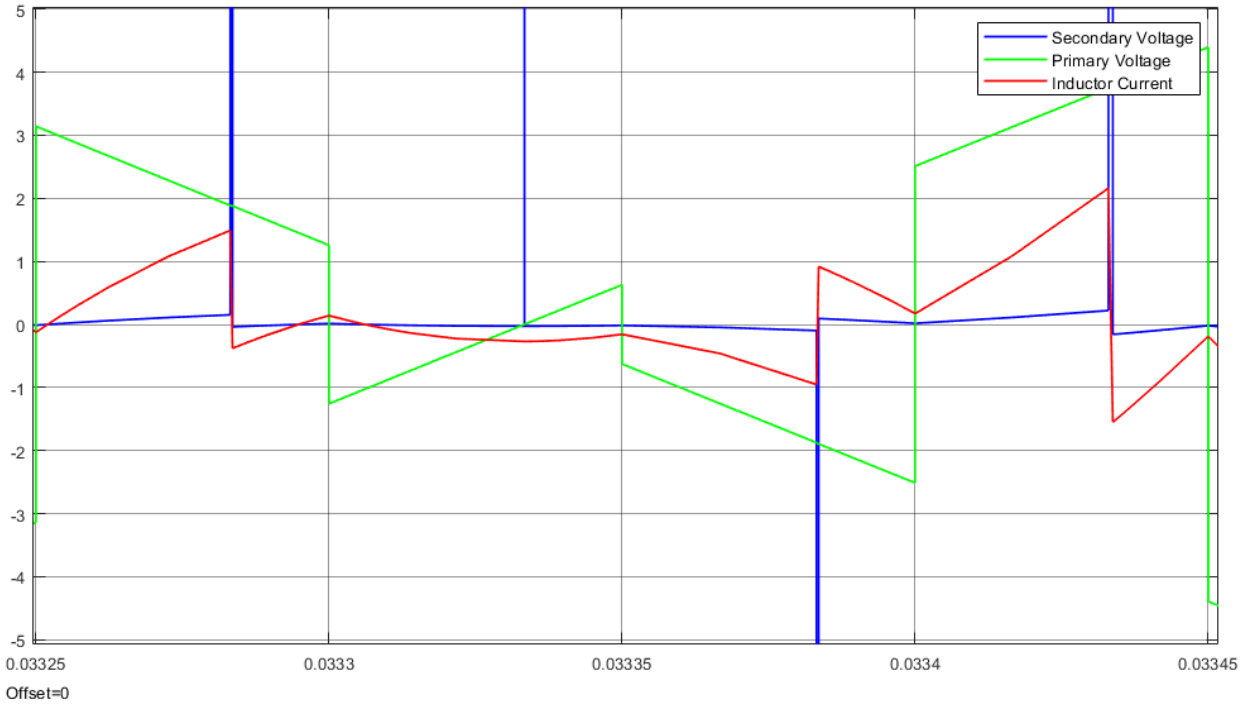

(d) Fourth Switching Point ($t = 2*T_i$).

Fig. 5.3: Comparison between Different Switching Points.

According to Fig. 5.3 (a)-(d), the inductor current (Red) in every different switching point was jumped showing non-linear current flow between two systems. These four different non-linear currents are complicated to compute. Defining an exact non-linear equation in this problem may be complicated. Thus, applying a random noise to the stable linear function is one way to achieve non-linear function approximately. To solve this problem, a random noise was generated and applied to two systems, $\dot{X}_1$ and $\dot{X}_2$. Then, by using concatenated two modeling method, two of 2-by-2 unstable matrix was derived to implement the switched system theory.

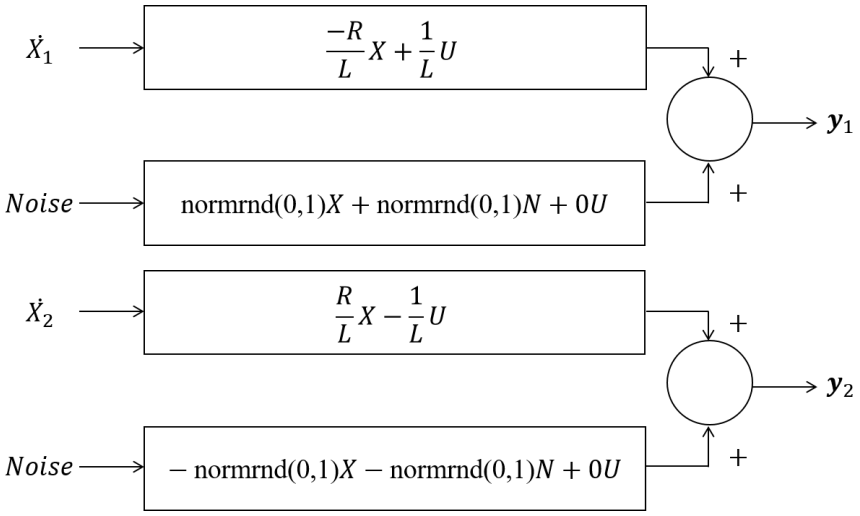

Fig. 5.4: Concatenating Method.

Here,

$$\boldsymbol{y}_1 = \begin{bmatrix} \frac{-R}{L} & 0 \\ \text{normrnd}(0,1) & \text{normrnd}(0,1) \end{bmatrix} \boldsymbol{X} + \begin{bmatrix} \frac{1}{L} \\ 0 \end{bmatrix} \boldsymbol{U} = \boldsymbol{A_1 X} + \boldsymbol{B_1 U}$$

and

$$\boldsymbol{y}_2 = \begin{bmatrix} \frac{R}{L} & 0 \\ \text{-normrnd(0,1)} & \text{-normrnd(0,1)} \end{bmatrix} \boldsymbol{X} + \begin{bmatrix} -\frac{1}{L} \\ 0 \end{bmatrix} \boldsymbol{U} = \boldsymbol{B_2 X} + \boldsymbol{B_2 U}.$$

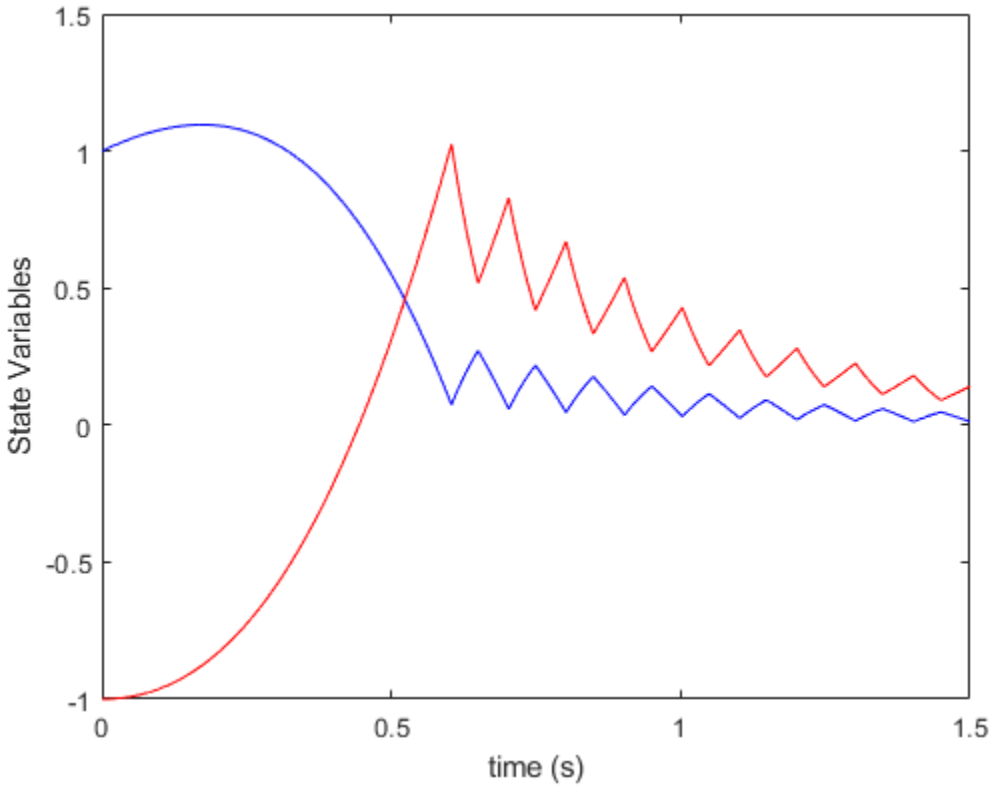

Fig. 5.5: State trajectories plotted as functions of time.

After multiple times of the simulation, the intended simulation result was achieved. The simulation of the two switched unstable system results in Fig. 5.5. Blue line is the first unstable system $\boldsymbol{A}_1$ of equation $\boldsymbol{y}_1$ and the red line is the second unstable system $\boldsymbol{A}_2$ of equation $\boldsymbol{y}_2$. The calculated results using Table (5.1) by MATLAB show that

$$\boldsymbol{A}_1 = \begin{bmatrix} \frac{-R}{L} & 0 \\ \text{normrnd(0,1)} & \text{normrnd(0,1)} \end{bmatrix} = \begin{bmatrix} -2000 & 0 \\ 0.8649 & 0.0301 \end{bmatrix}$$

$$\boldsymbol{A}_2 = \begin{bmatrix} \frac{R}{L} & 0 \\ \text{-normrnd(0,1)} & \text{-normrnd(0,1)} \end{bmatrix} = \begin{bmatrix} 2000 & 0 \\ \text{-0.1649} & -0.6277 \end{bmatrix}$$

and

$\boldsymbol{P}_{eq} = \begin{bmatrix} 0.0013 & -1.4146e-06 \\ \text{-1.4146e-06} & 1.8580 \end{bmatrix}$, where $\boldsymbol{P}_{eq}$ is the solution of Lyapunov function.

The simulation result shows that, as time goes on, two switched unstable systems asymptotically approach a steady state value of approximately 0.2.

5.3 Conclusion

In this chapter, the stability of the proposed converter as an application of switched systems is demonstrated by construction of Lyapunov function. To find a stable convex combination, random noise was generated for modeling non-linear functions. Finally, two unstable systems were simulated under the theoretical understanding and the simulation result showed that two unstable systems by switching eventually stabilized.

Chapter 6

Conclusion

For designing a universal and scalable grid power converter, a bi-directional dual-active bridge AC/DC power converter using H_∞ controller is developed and simulated. To design the H_∞ controller, the system transfer function should be obtained first. State-space averaging technique was used to obtain small-signal plant model for its transfer function. Then H_∞ controller was calculated by MATLAB and compared with the performance of PI controller. According to the simulation results, even though the PI controller applied to the proposed converter looks more effective than an H_∞ controller, we could not conclude which is better controller due to different simulated conditions by different approached PID and H_∞ theories. Thus finding a method to compare two controllers will be the future work. In addition to, the stability was verified using switched system theory by the construction of the Lyapunov function.

References

[1] N. D. Weise, G. Castelino, K. Basu, and N. Mohan, *A single-stage dual-active-bridge-based soft switched ac/dc converter with open-loop power factor correction and other advanced features*, IEEE Transactions on Power Electronics, vol. 29, no. 8, pp. 40074016, Aug 2014.

[2] G. Castelino, K. Basu, N. Weise and N. Mohan, *A bi-directional, isolated, single-stage, DAB-based AC-DC converter with open-loop power factor correct- ion and other advanced features*, 2012 IEEE International Conference on Industrial Technology, Athens, 2012, pp. 938-943.

[3] R. Baranwal, G. F. Castelino, K. Iyer, K. Basu and N.Mohan, *A Dual-Active-Bridge-Based Single-Phase AC to DC Power Electronic Transformer With Advanced Features*, IEEE Transactions on Power Electronics, vol. 33, no. 1, pp. 313-331, Jan. 2018.

[4] Weise, Nathan David. (2011). *Universal utility interface for plug-in hybrid electric vehicles with vehicle-to-grid functionality*.., Retrieved from the University of Minnesota Digital Conservancy, http://hdl.handle.net/11299/116540.

[5] Y. P. Chan, K. H. Loo and Y. M. Lai, *Single-Stage Resonant AC-DC Dual Active Bridge*

Converter with Flexible Active and Reactive Power Control, 2016 IEEE Vehicle Power and Propulsion Conference (VPPC), Hangzhou, 2016, pp. 1-6.

[6] N. Weise, *DQ current control of a bidirectional, isolated, single-stage AC-DC converter for vehicle-to-grid applications*, 2013 IEEE Power & Energy Society General Meeting, Vancouver, BC, 2013, pp. 1-5.

[7] Matthew Lackner, Anthony Rogers, and James Manwell. *Uncertainty Analysis in Wind Resource Assessment and Wind Energy Production Estimation, 45th AIAA Aerospace Sciences Meeting and Exhibit*, Aerospace Sciences Meetings, https://doi.org/10.2514/6.2007-1222

[8] Leo Rollins, "Robust Control Theory." Internet: https://users.ece.cmu.edu/~koopman/des_s99/control_theory/, Spring 1999 [Nov. 01, 2017].

[9] Benny Yeung. *Chapter 7 Dynamic Modelling and Control of DC/DC Converters*, Internet: ftp://ftp.ee.polyu.edu.hk/echeng/EE529_PowerElect_Utility/07.%20Dynamic%20Modelling%20and%20Control%20of%20DC-DC%20Converters%20(Benny%20Yeung).pdf [Feb. 01, 2017].

[10] Mirzaei, M., Poulsen, N. K., & Niemann, H. H. (2012). *Wind Turbine Control: Robust Model Based Approach*. Kgs. Lyngby: Technical University of Denmark. (IMM-PHD-2012; No. 281).

[11] Tennessee Tech University, *Chapter 2 Single Phase Pulse Width Modulated Inverters*, Internet: https://www.tntech.edu/files/cesr/StudThesis/asuri/Chapter2.pdf [Oct. 01, 2017].

[12] A.M. Gole, *Sinusoidal Pulse width modulation*, 24.437 Power electronics, 2000, Internet:

http://encon.fke.utm.my/nikd/SEM4413/spwm.pdf [Oct. 01, 2017]

[13] Georgios D. Demetriades, *On Small-Signal Analysis and Control of The Single- and The Dual-Active Bridge Topologies*, KTH, Stockholm, 2005. Internet: http://kth.diva-portal.org/smash/get/diva2:7434/FULLTEXT01.pdf.

[14] BoHyun Ahn and Vincent Winstead, *Small Signal Model Averaging of Bi-Directional Converter,* EIT Conference 2018, Rochester, Michigan, May 5, 2018, no. 227.

[15] R. D. Middlebrook and Slobodan Cuk, *A General Unified Approach to Modelling Switching-Converter Power Stages*, IEEE Power Electronics Specialists Conference, Cleveland, Ohio, June 8-10, 1976, pp. 73-86.

[16] W.P.M.H. Heemels, D. Lehmann, J. Lunze, and B. De Schutter, *Introduction to hybrid systems*, Chapter 1 in Handbook of Hybrid Systems Control – Theory, Tools, Applications (J. Lunze and F. Lamnabhi-Lagarrigue, eds.), Cambridge, UK: Cambridge University Press, ISBN 978-0-521-76505-3, pp. 3–30, 2009.

[17] Daniel Liberzon, *Switched Systems: Stability Analysis and Control Synthesis: Lecture Notes for HYCON-EECI Graduate School on Control*, Coordinated Science Laboratory, University of Illinois at Urbana-Champaign, U.S.A. Internet: http://liberzon.csl.illinois.edu/teaching/Liberzon-LectureNotes.pdf.

[18] D. Hernandez-Torres, O. Sename, D. Riu, and F. Druart, *On the Robust Control of DC-DC Converters: Application to a Hybrid Power Generation System*, 4th IFAC Symposium on System, Structure and Control (SSSC 2010), Sep 2010, Ancona, Italy.

[19] G. Weiss, Q.C. Zhong, and T.C. Green, *H_∞ Repetitive Control of DC-AC Converters in Microgrids*, IEEE Transactions on Power Electronics, Vol. 19, No 1, January 2004. Pp. 219-230.

[20] R. Naim, G. Weiss, and S. Ben-Yaakov, *H_∞ Control Applied to Boost Power Converters*, IEEE Transactions on Power Electronics, vol. 12, no. 4, July 1997.

[21] E. Vidal-Idiarte, L. Martinez-Salamero, H. Valderrama-Blavi, F. Guinjoan, and J. Maixe, *Analysis and Design of H_∞ Control of Nonminimum Phase-Switching Converters*, IEEE Transactions on Circuit and Systems-I: Fundamental Theory and Applications, vol. 50, no. 10, October 2003.

[22] E. Vidal-Idiarte, L. Martinez-Salamero, H. Valderrama-Blavi, and F. Guinjoan, *H_∞ Control of DC-to-DC Switching Converters*, in Proc. IEEE Int. Symp. Citcuits and Systems, ISCAS'99, vol. 5, 1999, pp. 238-241.

[23] Yan-hua Xian and Jiu-chao Feng, *Output Feedback H-infinity Control for Buck Converter with Unvertainty Parameters*, 2011 IEEE 13th International Conference on Communication Technology, Jinan, 2011, pp. 887-891.

[24] Andreas Kugi and Kurt Schlacher, Nonlinear *H_∞ -Controller Design for a DC-to-DC Power Converter*, IEEE Transactions on Control Systems Technology, vol. 7, no. 2, March 1999.

[25] D. Hernandez-Torres, O. Sename, D. Riu, and F. Druart, *On the Robust Control of DC-DC Converters: Application to a Hybrid Power Generation System*, 4th IFAC Symposium on System, Structure and Control (SSSC 2010), Sep 2010, Ancona, Italy.

[26] K. Zhou and J. C. Doyle, *Essentials of Robust Control*, Prentice-Hall, 1998

[27] Mark A. Wicks et al, *Construction of Piecewise Lyapunov Functions for Stabilizing Switched Systems*, Proceedings of the 33rd IEEE Conference on Decision and Control, Lake Buena Vista, Florida, December 1994, pp. 3492-3497.

[28] Mark A. Wicks et al, *Structured Rank-Reducing Matrix Perturbations: Theory and Computation*, American Control Conference, 1992, pp. 649-653.

[29] Yimin Lu et al, *Hybrid Feedback Switching Control in a Buck Converter*, 2008 IEEE International Conference on Automation and Logistics, Qingdao, China, September, 2008, pp. 207-210.

[30] Paolo Bolzern et al, *Quadratic stabilization of a switched affine system about a nonequilibrium point*, proceeding of the 2004 American Control Conference, Boston, Massachusetts, June 30-July 2, 2004, pp 3890 – 3895.

[31] MathWorks, "augw." Internet: https://www.mathworks.com/help/robust/ref/augw.html [Oct. 20, 2018].

[32] Voltech, "Measuring Leakage Inductance", Internet: http://www.voltech.com/Articles/104-105/1_What_is_Leakage_Inductance [Jun. 18, 2018].

Appendix A

Leakage Inductance

The concept of the leakage inductance is studied in [32]. An ideal transformer is lossless and perfectly coupled. In other words, all of magnetic flux in the ideal transformer flows between the primary winding and the secondary winding completely. However, a real transformer losses some of the magnetic flux between the primary winding and the secondary winding. The lost flux, “leakage flux”, in the real transformer should be compensated for an additional inductor, “leakage inductance” that is in series with the primary or secondary winding to operate the transformer accurately. If there exists an air gap in the core of real transformer, larger leakage inductance is required.

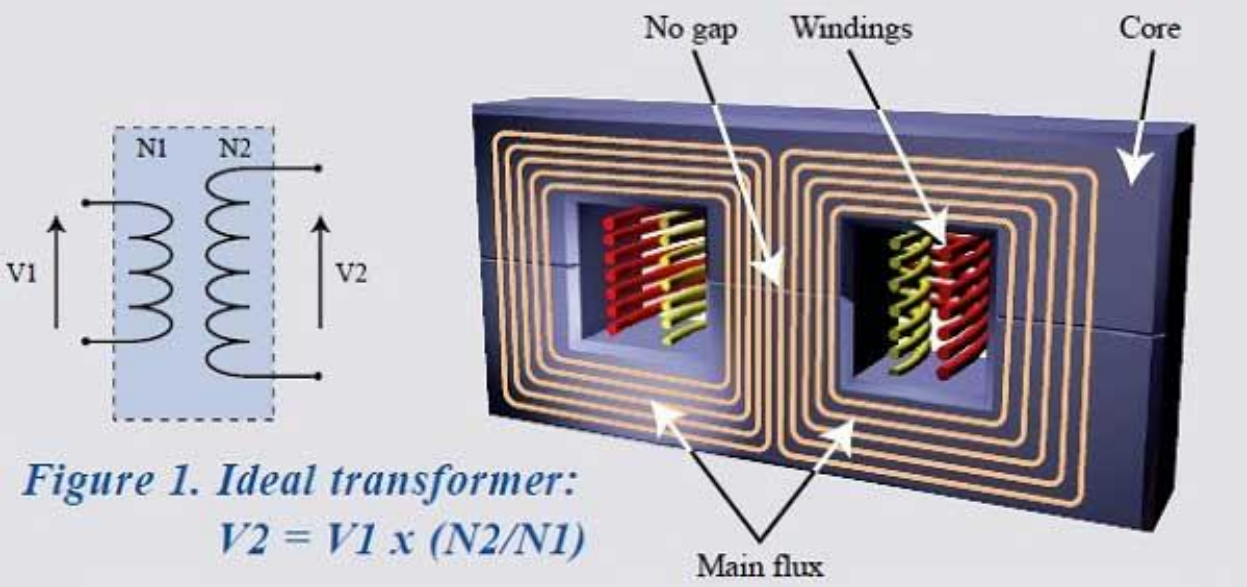

Figure 1. Ideal transformer:
V2 = V1 x (N2/N1)

<Ideal Transformer>

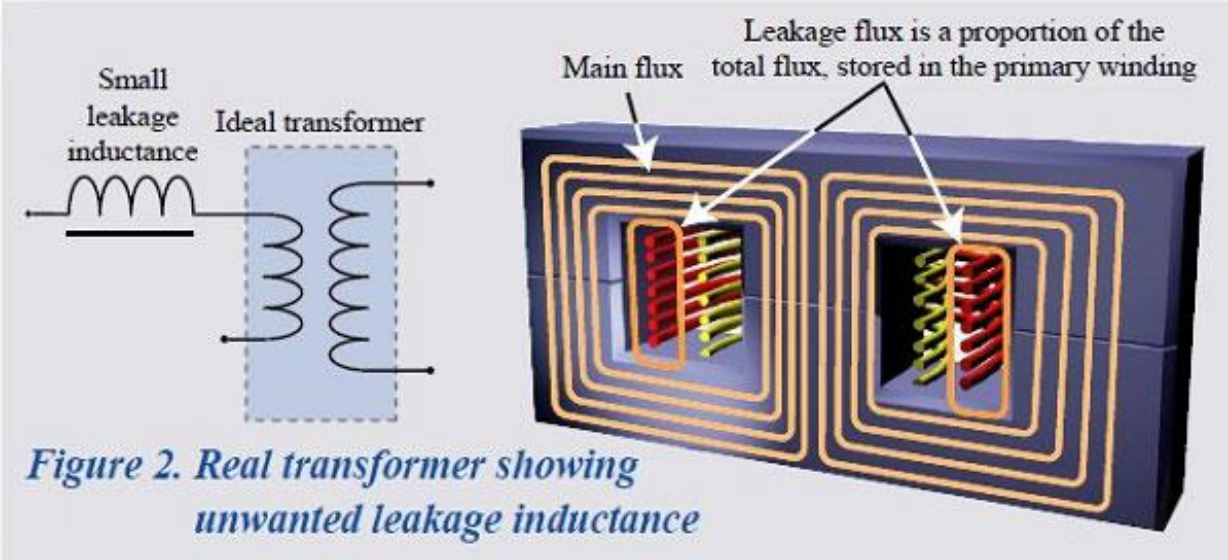

Figure 2. Real transformer showing
unwanted leakage inductance

<Real Transformer>

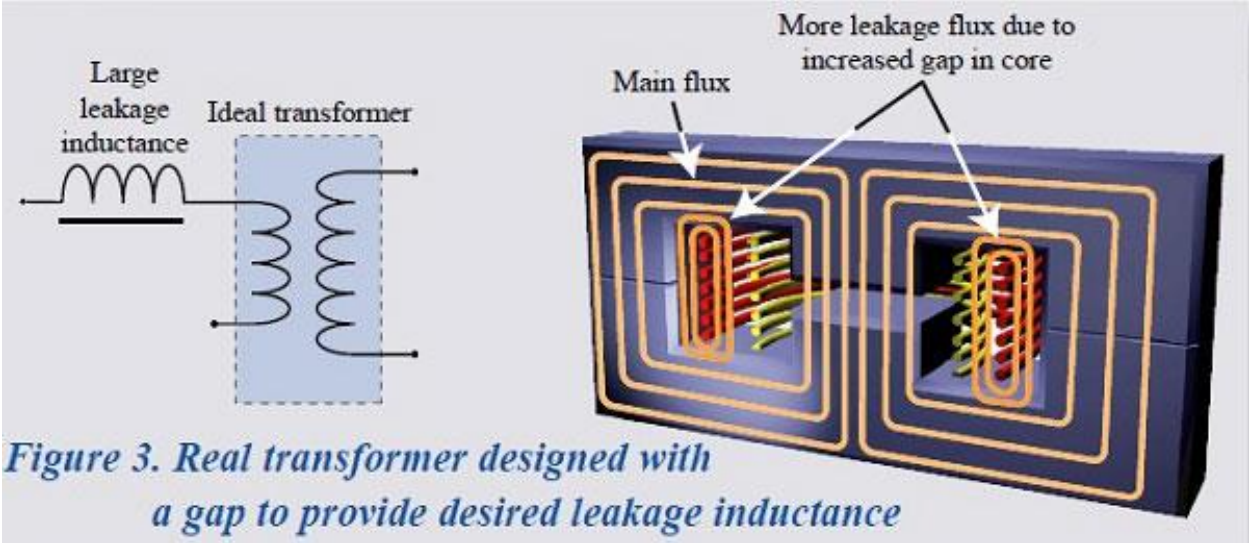

Figure 3. Real transformer designed with a gap to provide desired leakage inductance

<Real Transformer with an Air Gap>